LAWRENCE
LIVERMORE
NATIONAL
LABORATORY

LLNL-TR-729310

Propagation of a Strong Shock Over a Random Bed of Spherical Particles

K. Salari

April 18, 2017

Disclaimer

This work performed under the auspices of the U.S. Department of Energy by Lawrence Livermore National Laboratory under Contract DE-AC52-07NA27344.

Propagation of a Strong Shock Over a Random Bed of Spherical Particles

Y. Mehta[1], C. Neal[1], K. Salari[2], T.L. Jackson[1], S. Balachandar[1], and S. Thakur[1]

[1] *Department of Mechanical and Aerospace Engineering, University of Florida, Gainesville, FL 32611*
[2] *Lawrence Livermore National Laboratory*

February 6, 2017

Abstract

Propagation of a strong shock through a bed of particles results in complex wave dynamics such as a reflected shock, a transmitted shock, and highly unsteady flow inside the particle bed. In this paper we present three-dimensional numerical simulations of shock propagation in air over a random bed of particles. We assume the flow is inviscid and governed by the Euler equations of gas dynamics. Simulations are carried out by varying the volume fraction of the particle bed at a fixed shock Mach number. We compute the unsteady inviscid streamwise and transverse drag coefficients as a function of time for each particle in the random bed as a function of volume fraction. We show that (i) there are significant variations in the peak drag for the particles in the bed, (ii) the mean peak drag as a function of streamwise distance through the bed decreases with a slope that increases as the volume fraction increases, and (iii) the deviation from the mean peak drag does not correlate with local volume fraction. We also present the local Mach number and pressure contours for the different volume fractions to explain the various observed complex physical mechanisms occurring during the shock-particle interactions. Since the shock interaction with the random bed of particles leads to transmitted and reflected waves, we compute the average flow properties to characterize the strength of the transmitted and reflected shock waves and quantify the energy dissipation inside the particle bed. Finally, to better understand the complex wave dynamics in a random bed, we consider a simpler approximation of a planar shock propagating in a duct with a sudden area change. We obtain Riemann solutions to this problem, which are used to compare with fully resolved numerical simulations.

1 Introduction

The study of shock interaction with particles has been largely motivated because of its wide ranging applications in engineering systems and natural phenomena. It has applications in drug delivery systems [1], volcanic eruptions, dust storms in mines, supernovae and explosive dispersal of particles using a smoke grenade. Shock interaction with a bed of particles has also been studied to predict blast wave attenuation using porous media to design products for blast wave mitigation. The complex interaction between the compressible flow features, such as shock wave and expansion fan, the dispersed phase, and the resulting turbulence makes these multiphase flows very difficult to predict and control. Furthermore, these problems encompass a wide range of spatial and temporal scales resulting in challenges for modeling and numerical simulations. Experimental measurements of high speed multiphase flows are also fraught with difficulties. Nonetheless, the problem of

shock interactions with particles has been actively researched using different computational and experimental approaches over last couple of decades.

Multiple experiments and numerical solutions have been carried out to investigate the problem of shock particle interaction. At the level of an isolated particle, Igra, Britan, Takayama, Tanno and Sun *et al.* [2–6] have carried out experiments and simulations to report the unsteady drag experienced by a particle during shock impingement. Parmar *et al.* [7–9] rigorously solved the linearized compressible Navier-Stokes equations to obtain a model that accurately predicts the unsteady force on the particle during shock propagation, that compared well with the experimental data reported by Sun *et al.* [6]. More recently, a number of numerical solutions of shock interaction with multiple particles have been reported. Lu *et al.* [10] performed direct numerical simulations of shock interaction with a cloud of particles and built a multi-scale model using neural network to predict the particle motion. Regele *et al.* [11] carried out two-dimensional simulations of shock interaction with cylinders. They reported a pressure drop inside the bed and reduced the two-dimensional phase-averaged information to a one-dimensional model to predict the flow behavior. They also highlighted the effect of Reynolds stress induced in the flow because of the presence of the particles. Collins *et al.* [12] reported the flow field fluctuations during shock interaction with randomly distributed foam fibers and investigated collapse of foam fibers and eventual mixing caused by unsteady flow in the particle bed. Sridharan *et al.* [13] considered shock propagation over a streamwise array of particles and investigated the effect of particle spacing and shock Mach number on the drag experienced by the array of particles. They reported increase in the peak drag coefficient as the shock traveled deep into the array. Mehta *et al.* [14] carried out simulations of shock interaction with a one-dimensional transverse array of particles and reported that temporal deviations in the drag coefficient from that of a single particle can be correlated to the acoustic-particle interaction time. More recently Mehta *et al.* [15] performed fully resolved three-dimensional numerical investigation of shock interacting with structured array of particles. They examined the effect of shock Mach number and volume fraction on the drag experienced by the particles. They also reported pressure fluctuations inside the particle bed and pressure attenuation behind the particle curtain.

When an incident shock encounters a particle bed, one of the primary effects of the particle bed is to act as a sudden contraction, since the area of cross-section for the flow rapidly decreases from 100% to $(100 - \phi_1)\%$ across the leading front of the bed, where ϕ_1 is the volume fraction of particles within the bed. If we ignore for the moment the role of particles in diffracting the shock wave and the resulting momentum exchange between the particles and the flow, we can simplify the problem as a planar shock propagating in a duct with a sudden area reduction. We note that an analytical solution of the Riemann problem for a duct with a sudden change in cross-sectional area has recently been obtained by [16–18]. Unlike the standard problem of a planar shock tube of uniform cross-section, with a sudden area change, a total of four different waves (a combination of shocks, expansion fans, contact discontinuity and stationary wave) propagate upstream and downstream. A variety of possible flow configurations, including the possibility of resonance, has been shown to exist. Resonance occurs when different elementary waves are not well separated and they coincide.

Here, we exploit these general Riemann solutions in the context of a strong shock propagating into a particle bed. After the incident shock encounters the leading front of the particle bed, a reflected wave travels upstream of the particle bed and a transmitted shock travels downstream through the particle bed. The strength and nature of the reflected wave, whether it is a shock wave or an expansion fan, depends on parameters such as the incident shock strength and the volume fraction of the particle bed. On average the strength of the transmitted shock is less than that of the incident shock, i.e., shock interaction with a particle bed results in pressure attenuation

behind the particle bed [19, 20]. However, it has been observed in case of shock propagation through a structured array of particles or rods that there are localized regions within the array where the shock pressure could be amplified due to constructive interference or shock focusing [21]. Recent three-dimensional simulations have however shown that the overall effect is to weaken the transmitted shock because of energy dissipation inside the particle bed [15]. In this work we will obtain solutions of the corresponding Riemann problem considering only the effect of the area reduction. These solutions show the nature of waves other than the reflected and transmitted shocks to propagate through the bed. The Riemann solutions can then be compared to those of numerical simulations of shock propagation through a bed of particles to highlight the role of particles in diffracting the flow.

For an isolated spherical particle the critical Mach number is 0.6. If the Mach number based on relative velocity between the oncoming flow and the particle exceeds the critical Mach number, the flow as it negotiates around the particle becomes supersonic around the particle resulting in the formation of shocklets. If the Mach number of the oncoming flow is greater than unity, a bow shock will form ahead of the particle. In the case of an incident shock wave in air, for shock Mach numbers less than 1.50, the Mach number of the post-shock uniform flow is below critical. Incident shock Mach numbers greater than 1.50 will result in the formation of shocklets during the post-shock flow. For incident shock Mach numbers greater than 2.0 there will be a bow shock forming ahead of the particle. These results are for shock propagation past an isolated particle. The behavior is expected to qualitatively remain the same even for a distribution of particles. The critical values of incident shock Mach number that will result in the formation of shocklets and bow shocks can be expected to decrease with increasing particle volume fraction. Nevertheless, when present, the bow shocks and local shocklets contribute to energy dissipation, which is in addition to dissipation due to viscous mechanisms as the flow goes through the bed of particles.

As the transmitted shock travels inside the particle bed, each individual particle inside the bed diffracts the shock wave and radiates out compression and expansion waves. Waves from individual particles interact, resulting in a complex flow inside the bed. This complex wave interaction results in large unsteady fluctuation of flow quantities inside the bed. Currently there is very little understanding regarding the strength and nature of these inviscid fluctuations. Flow field fluctuations have a big impact on momentum and heat transfer between the continuous and dispersed phases. There is a need to resolve these fluctuations and understand their relation to the interphase momentum and energy coupling. Viscous effects add to this complexity with the formation of boundary layers and vortical wakes behind individual particles. A bed of particles will lead to wake-wake and wake-particle interactions as well.

To understand the effect of shock wave on the forces experienced by the particle and the back effect of particles on the flow, here we will specifically consider the problem of a planar shock encountering a randomly distributed bed of spherical particles. We have carried out fully resolved three-dimensional direct numerical simulations of shock interaction with randomly distributed spherical particles. The particle volume fraction, ϕ_1, is varied as $10\%, 15\%, 20\%$ and 25%. The simulations to be reported here are inviscid in nature, and furthermore the particles are held fixed in position during the simulation. Thus, the applicability of the present work is limited to the short time immediately following the passage of the transmitted shock. As pointed out in Mehta *et al.* [15], during this early period the inviscid mechanisms dominate the flow and the forces experienced by the particle. Also, for large particle-to-gas density ratios, during this early period of transmitted shock propagation, the particles can be assumed nearly stationary.

We start with a planar incident shock of Mach number 3, which propagates inside the particle bed. This planar wave is then distorted as it travels through the bed, resulting in spatial and temporal fluctuations in the transmitted shock wave front. These fluctuations in shock wave front

result in variations in drag experienced by the particles. In other words, as the transmitted shock wave propagates through the bed, there will be substantial particle-to-particle variation in their aerodynamic forces. These force variations are not correlated to local volume fraction but depend on the precise location of neighboring particles. For example, a particle shielded by an immediate upstream neighbor will experience drag reduction, wheres a particle whose upstream neighbor contributes to shock focusing and a substantial increase in drag. Currently there does not exist any analytical model which can explain or capture these particle-to-particle variations in drag force. The complex three-dimensional flow within the bed also leads to transverse forces on the individual particles. However, when averaged over a large number of particles, we expect the average to approach zero, since the transverse force on individual particles is randomly oriented depending on the location of its neighbors. Dissipation of energy leads to weakening of the transmitted shock leading to a decrease in peak drag force experienced by the particles deeper in the bed. We compare this reduction in drag force for random pack of particles with reduction in drag force experienced by the particles arranged in structured arrays. We also compute cross-section averaged flow field quantities such as pressure, density, and streamwise velocity and transverse velocity to quantify the level of pseudo-turbulence within the particle bed.

This paper is organized as follows. The governing equations, computational setup, and a grid resolution study are presented in Section 2. The Riemann solution for a planar shock propagating in a duct is presented in Section 3. The results are presented in Section 4. Here, we compute the streamwise and transverse forces as a function of time for each particle in the bed as the transmitted shock propagates through the bed. We also discuss the flowfield and the pressure attenuation through the bed. Finally, to gain a deeper understanding of the dynamics as the imposed shock propagates into the bed, we compare numerical solutions with the Riemann solution of a planar shock propagating in a duct. Finally, conclusions are given in Section 5.

2 Basic Model

2.1 Governing Equations

In this paper we investigate shock-particle interactions, where the interactions are dominated by inviscid mechanisms and so viscous and thermal effects are ignored. For a discussion of relevant time scales, see [15]. The appropriate three-dimensional equations governing an inviscid fluid are therefore given by

$$\frac{\partial \rho}{\partial t} + \nabla \cdot (\rho \vec{u}) = 0, \tag{1}$$

$$\frac{\partial (\rho \vec{u})}{\partial t} + \nabla p + \nabla \cdot (\rho \vec{u} \vec{u}) = 0, \tag{2}$$

$$\frac{\partial E}{\partial t} + \nabla \cdot ((E + p)\vec{u}) = 0, \tag{3}$$

where ρ is the density, $\vec{u} = (u, v, w)$ the velocity, p the pressure, and E the total energy per unit volume given by

$$E = \rho(e + \frac{1}{2}\vec{u} \cdot \vec{u}), \tag{4}$$

where e is the internal energy. In this work we assume an ideal gas, for which $p = (\gamma - 1)\rho e$ with properties $\gamma = 1.4$, $c_p = 1004.6$ J/kg-K, and $R = 287.04$ J/kg-K.

2.2 Numerical Method

For the numerical simulations we use a finite volume solver on a body conforming unstructured grid. A random distribution of monodispersed spheres in a rectangular box, as shown in Fig. 1(a) is considered. The region of gas flow exterior of the spheres is discretized with a well-resolved unstructured grid. A second order accurate AUSM+ [22] scheme is used for the flux computation and the gradients are modified using a weighted essentially non-oscillatory (WENO) reconstruction technique [23]. Time integration is performed using third order Runge-Kutta method. This code has been tested and validated previously for numerous problems involving compressible flows with shock-waves. Validation and verification of the numerical scheme can be found in [7, 24–26].

During the passage of the shock, the particles are assumed to remain rigid and immobile during the short duration of the simulations. The configuration shown in Fig. 1(a) can thus serve as a good approximation for shock propagation through a porous medium. We also consider this configuration to well approximate shock propagation through a random dispersion of spherical particles. The short-lived transient force created as the shock interacts with the particle, imparts a near impulsive force on the particle. If the particle was allowed to freely move, as shown by Ling *et al.* [26], the ratio of change in particle velocity due to this impulsive force to that of fluid velocity across the shock scales as fluid-to-particle density ratio. For example, for aluminum particle in air, the density ratio is $O(1000)$ and the initial impulsive gain in particle velocity is small. The timescale associated with significant particle movement is therefore relatively long due to the large inertia of the particle (particle-fluid density ratio is large). Thus, for the situation and time scales considered here, it is reasonable to ignore particle movement.

2.3 Drag

The drag coefficient is defined by

$$\vec{C}_D = \frac{\vec{F}}{\frac{1}{2}\rho_6 u_6^2 A}, \tag{5}$$

where $\vec{F}$ is the force, ρ_6 the post incident shock density, u_6 the corresponding post incident shock velocity, and A the cross-section of the particle. For a sphere, $A = \pi d_p^2/4$, where d_p is the particle diameter. Note that since we are carrying out inviscid simulations, only the pressure contributes to the force. The force components are therefore given by

$$F_i = \vec{F} \cdot \hat{e}_i \equiv \int_{S_p} p\, \hat{n} \cdot \hat{e}_i \, dS, \tag{6}$$

where $\hat{e}_i$ is the unit vector in the x_i-direction, $\hat{n}$ the outward pointing normal, and S_p the surface of the particle. In this way the drag coefficients in the (x, y, z)-directions are given by

$$C_D = \frac{F_x}{\frac{1}{2}\rho_6 u_6^2 A}, \qquad C_{L,y} = \frac{F_y}{\frac{1}{2}\rho_6 u_6^2 A}, \qquad C_{L,z} = \frac{F_z}{\frac{1}{2}\rho_6 u_6^2 A}. \tag{7}$$

The total transverse drag coefficient is given by $C_L^2 = C_{L,y}^2 + C_{L,z}^2$, and the total drag coefficient is given by $C_{D,T}^2 = C_D^2 + C_{L,y}^2 + C_{L,z}^2$.

2.4 Geometry, Simulation Setup, and Boundary Conditions

In this paper we consider particles placed randomly in a three-dimensional rectangular box; the computational domain and distribution of particles for a fixed volume fraction of 10% can be seen

in Fig. 1(a). The computational domain has equal y and z edge lengths, with an extended x length that is in the direction of the flow. The computational domain shown in Fig. 1(a) can be separated into two distinct regions: (i) A shocked air side that is upstream of the imposed shockwave (the state in this region is denoted by ⑥), and (ii) a pre-shocked quiescent ambient air into which the imposed shockwave is moving (the state in this region is denoted by ①). The two regions are marked in Fig. 1(b).

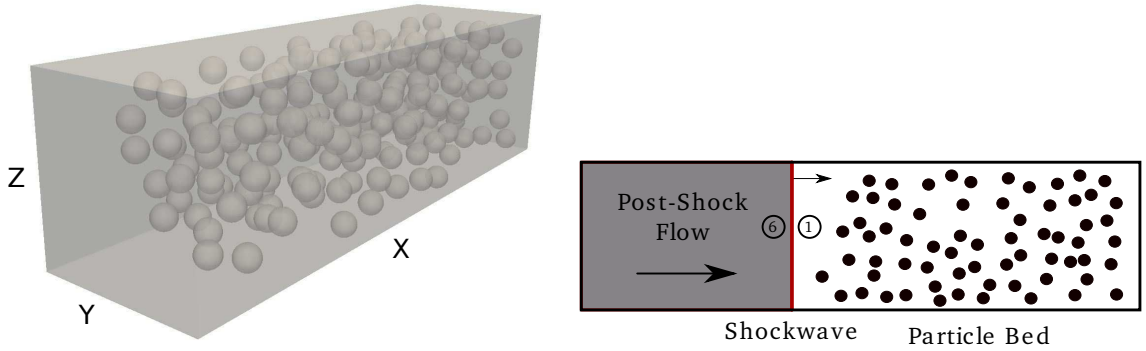

(a) (b)

FIG. 1: (a) Diagram of computational domain with 200 rigid particles randomly dispersed. (b) Imposed shock wave moving into a bed of particles.

Since we are solving the inviscid equations, there are only a few relevant length scales in the problem. These are the particle diameter, the mean inter-particle distance, and the length scale associated with the unit cell of the particle bed. The mean inter-particle distance is related to global particle volume fraction defined by

$$\phi_1 = \frac{V_p N_p}{V_c} \,. \tag{8}$$

We fix the particle diameter $d_p = 100$ μm, with the volume of a particle defined by $V_p = (\pi/6)d_p^3$. Here, N_p is the total number of particles within the computational domain and V_c is the volume of the unit cell that contains the the N_p particles. The domain is chosen to be 8 particle diameters in length along the y and z directions. Along the streamwise direction the computational domain is separated into an upstream region without particles and a downstream region containing a random distribution of particles. The streamwise length of the computational domain containing the particles is chosen to be about 12 particle diameters, whose precise value are chosen such that as the particle volume fraction varied from 10% to 25%, the number of particles within the computational domain varied from 200 to 500 respectively. Particles are randomly placed within the downstream section of the computational domain with the following two constraints: (i) a minimum allowable inter-particle spacing is maintained at $d_p/20$, and (ii) a minimum allowable spacing between a particle and the domain walls along the y and z directions is also maintained at $d_p/20$.

The pre-shock state is quiescent ambient air with $p_1 = 101.325$ kPa and $\rho_1 = 1.2048$ (kg/m^3). The post-shock conditions for air for a shock Mach number of $M_s = 3.0$, as determined by the Rankine-Hugoniot relations for an ideal gas with $\gamma = 1.4$ and $R = 287.04$ J/kg-K, are $p_6 = 1047.025$ kPa, $T_6 = 784.951$ K, $\rho_6 = 4.647$ kg/m^3, and $u_6 = 762.529$ m/s. The post-shock Mach number is $M_6 = 1.36$. The shock speed in the absence of particles is $u_s = 1029.678$ m/s. Note that the

post-shock pressure p_6 in air remains well below the yield strength for most materials (0.2 GPa), and so we do not expect the particles to deform.

For each volume fraction the simulation domain length in the streamwise x-direction is chosen large enough to avoid disturbances/reflections from upstream and downstream boundaries. The upstream boundary is treated as constant inflow boundary with inflow at post-shock properties, while all other boundaries, including the particle surfaces, are treated as slip walls.

2.5 Data Analysis

We characterize the randomized particle bed by generating a three-dimensional Voronoi tessellation of the domain where the centers of the Voronoi cells are the centers of the particles in the computational domain. Fig. 2 shows a sample Voronoi tessellation of a random particle bed for a 25 percent volume fraction bed. The orange lines in Fig. 2 mark the boundaries of the Voronoi cells. The blue objects are the particles in the domain. Thus, each particle is associated with a Voronoi cell and the number of Voronoi cell faces corresponds to the number of closest neighbors. By definition, all points within the Voronoi cell are closer to the corresponding particle than all the neighbors. The size of the Voronoi cell around each particle gives a measure of how much personal space each particle has as dictated by the location of its nearest neighbors and hence, provides information about the local volume fraction that is associated with each particle. This local volume fraction was computed for each particle in every simulation. The equation used to calculate the local volume fraction of the i^{th} particle is given by

$$\phi_i = \frac{V_p}{V_{V,i}}. \tag{9}$$

where $V_{V,i}$ is the Voronoi volume associated with the i^{th} particle. Each simulation for a different volume fraction has a unique distribution of particles. Even for the same volume fraction, different realizations with different distribution of particles can be considered. The distribution of particles within the computational domain will result in a unique distribution of local volume fractions associated with the particles. The mean, standard deviation, minimum and maximum values of the local volume fraction based on Voronoi volumes for the different simulations are tabulated to provide additional characterization of the different particle distributions. These values are provided in Table I. By definition $\sum_{i=1}^{N_p} V_{V,i} = V_c$, and as a result it can be seen that the mean local volume fraction based on Voronoi cells will not be precisely equal to ϕ_1. As can be seen from the table the difference between the two definitions of mean volume fraction is small, but non-zero. At $\phi_1 = 10\%$ the standard deviation is about 36% of the mean volume fraction and with increasing volume fraction the standard deviation decreases to about 22% of the mean at $\phi_1 = 25\%$. This reduction is consistent with the fact that with increasing volume fraction there is less freedom in the relative position of the neighboring particles. Observe that for $\phi_1\%$ the volume of the smallest Voronoi cell is only 30% of the mean and the largest Voronoi cell is 250% of the mean, indicating large variations in the local volume fraction, even though the particles are randomly distributed with uniform probability. The level of variation decreases with increasing ϕ_1, but remains substantially large even at $\phi_1 = 25\%$. Another way to quantify this local volume fraction variation is given by

$$\phi_{flu_i} = \frac{\phi_i - \phi_1}{\phi_1}, \tag{10}$$

which is just the relative difference between the local volume fraction of the Voronoi cell and the packing fraction.

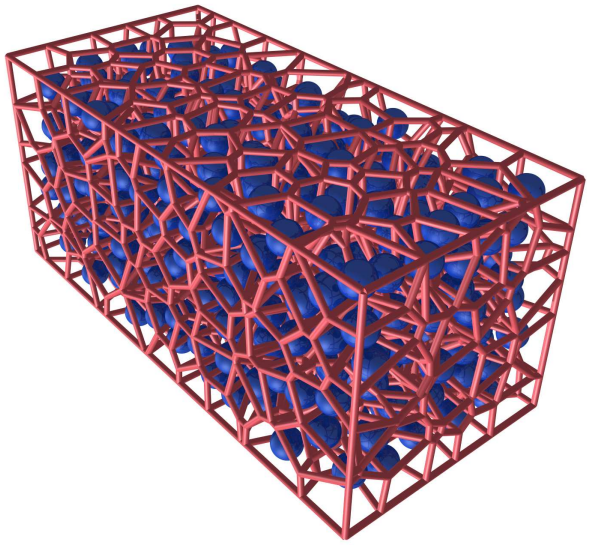

FIG. 2: Voronoi tessellation of the domain with 500 randomly placed particles; volume fraction 25%.

TABLE I: Statistics of the Voronoi cell volume fractions for different volume fraction grids. The columns correspond to (1) volume fraction ϕ_1 as defined by equation (8); (2) the mean volume fraction as determined from Voronoi tessellation; (3) the standard deviation; (4,5) the minimum and maximum volume fractions based on equation (9). Note that all quantities are in percentages.

Volume Fraction	Mean Volume Fraction	Std Volume Fraction	Min Volume Fraction	Max Volume Fraction
10	10.75	3.88	3.09	24.81
15	15.59	4.65	5.07	29.53
20	19.94	4.53	8.03	31.08
25	24.78	5.38	10.07	38.43

2.6 Grid Resolution

Unstructured tetrahedral grids are used for carrying out the fully resolved three-dimensional simulations of a shock propagating over a random bed of particles. DistMesh [27] is used to generate the mesh on the surface of the spherical particles. Once a surface mesh is created around the particles, TetGen [28] is used to generate the body-conforming unstructured tetrahedral mesh inside the simulation domain. The quality and size of the elements in the domain determines the sharpness of the shock and the accuracy of the solution. Similarly, adequate mesh resolution on the particle surface is required to properly compute aerodynamic forces, which are determined by integrating the pressure on the surface of each particle. The quality and size of the elements are controlled by monitoring the element aspect ratio and maximum element volume. Surface mesh resolution is controlled by specifying the maximum element area.

Previously, a grid resolution study was performed for a face-centered cubic (FCC) array of particles to determine the effect of these two constraints, the size of the elements in the domain and the surface mesh resolution per particle, on the solution [15]. Various grids were generated by varying the volume mesh and the surface mesh. For each mesh, the drag coefficient was compared to that of a well resolved simulation for shock propagation past a single isolated particle. In this way the error as a function of resolution was quantified. Based on the resolution study for the FCC array, we selected an appropriate mesh that balanced convergence of the peak drag coefficient with computational costs. We then generated unstructured grids for volume fractions of 10, 15, 20, and 25%. The total cell count for the grids and the number of particles in the random bed as a function of volume fraction are shown in Table II.

TABLE II: Tetrahedral cell counts and number of particles for different volume fractions.

Volume Fraction	Number of Tet Elements	Number of Particles
10	16,316,466	200
15	17,462,616	300
20	18,588,773	400
25	19,702,876	500

To determine the adequacy of the grid used in these simulations, we show in Fig. 3 a plot of the drag coefficient as a function of nondimensional time t/τ for a single isolated particle (red) with that of the first particle in the random bed (black). Here, τ is the shock-particle interaction time defined by

$$\tau = d_p/u_s, \tag{11}$$

where u_s is the shock speed and d_p is the particle diameter. The metrics that can be compared between the two simulations are the initial rise of the drag coefficient, the peak value of the drag coefficient, and the initial decay of the drag coefficient as the shock passes over the particle. From the figure we note that (i) both the initial rise and the initial decay in the drag coefficient compares well with that of the single particle; (ii) there is a small deviation of about 2% in the value of the peak drag coefficient; and (iii) that the time that the peak occurs is slightly shifted from that of the single particle result. The time shift in the peak and the difference in peak values are due to the reduced mesh resolution of each particle compared to the resolution used for the isolated particle. This reduction was necessary to keep the simulation at a reasonable size and cost. Also from the figure we see that for $t/\tau > 2$ the drag coefficient of the leading particle deviates from the drag coefficient of the isolated particle. This is because of the interactions of the shock reflections off the adjacent particles that occur in the random particle pack simulation. In other words, the

time history of the force on the leading particle at later times is influenced by the presence of the neighboring particles.

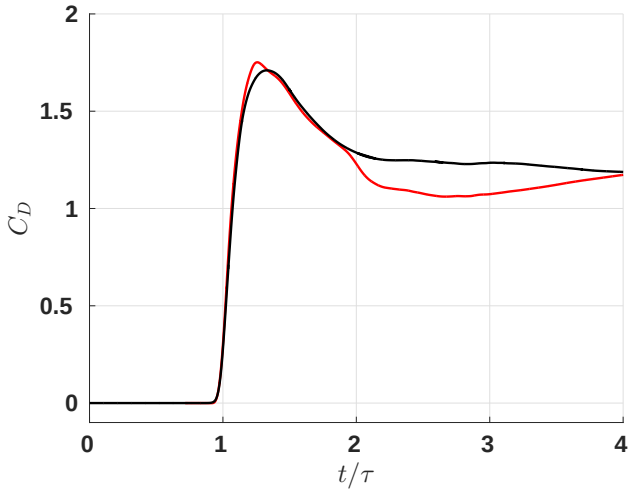

FIG. 3: Plot of streamwise drag, C_D, as a function of non-dimensional time, t/τ for isolated particle (red) and the leading particle in the random pack (black); $M_s = 3$.

3 Riemann Solution

Before we proceed to the analysis of the simulation results for a shock propagating through a random bed of particles, in this section we will first consider the simpler approximation of a planar shock propagating in a duct with a sudden area reduction. The instant when the incident shock is positioned exactly at the location of area reduction is shown in Fig. 4(a), with the pre-shock ambient state on the right marked by ① and the post-shock high-pressure state on the left marked by ⑥. The area to the left is taken to be $A_6 = 1$, and the area to the right is set as $A_1 = 1-\phi_1$. The left and the right states are related through the Rankine-Hugoniot relations for the incident shock of Mach number M_s. Fig. 4(b) then represents a Riemann problem, where across an imaginary diaphragm located at $x = 0$ we have the classic problem of a jump in the flow state represented by velocity, pressure and density, but in addition we also have a jump in the cross-sectional area. The solution to this Riemann problem can be obtained by solving equations (1-3), along with the following equation for the volume fraction evolution

$$\frac{\partial \phi}{\partial t} = 0\,, \tag{12}$$

which simply states that the initial area change remains unchanged over time.

The above Riemann problem represented by Fig. 4(a) has been recently investigated by [16–18]. These investigations are more general than the particular case of an imposed shock propagating through a duct of sudden area reduction, as they presented solutions for any combination of values for gas velocity, pressure, density, and change in cross-sectional area across the diaphragm. In particular, Han *et al.* [18] classified the general solution into six basic cases for the left-to-middle (L-M) waves and a matching six basic cases for the right-to-middle (R-M) waves, which taken together covers all solutions for all possible initial conditions. The six L-M cases are differentiated according to (i) whether the flow in state ⑥ is supersonic or subsonic, and (ii) the ordering of two different areas A_s and A_T (defined below) with respect to A_6 and A_1. The six R-M cases on the right

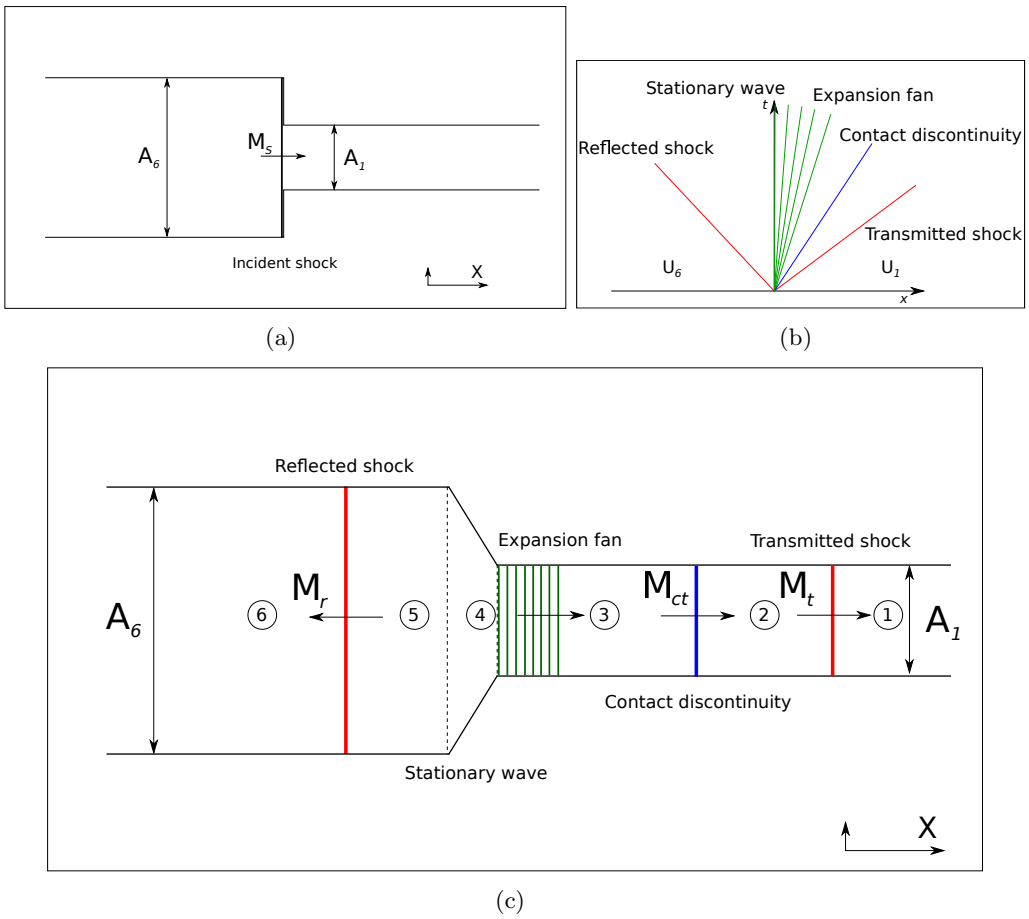

(a) (b)

(c)

FIG. 4: Plot of (a) 1-D setup of shock propagation over discontinuous area change, (b) wave configuration based on initial data, and (c) approximate locations of waves in the domain.

are differentiated similarly. In the absence of resonance there are four waves: a stationary wave with three other elementary waves that can be a shock wave, expansion fan, or a contact discontinuity. For some initial conditions the solution exhibits resonance, which results in a complex resonant wave with two other elementary waves.

Here we apply this general theory for the present case of the post-shock state ⑥ on one side and pre-shock ambient state ① on the other side of the sudden area reduction, as shown in Fig. 4(a). Let the gas velocity, pressure, density, and speed of sound in the left state be u_6, p_6, ρ_6, and c_6, respectively. The corresponding values on the right are u_1, p_1, ρ_1, and c_1. Values for our problem for a Mach 3.0 shock wave moving into quiescent ambient are given in Table III. For this case the post-shock flow on the left is supersonic, therefore $u_6 - c_6 > 0$ and also $u_1 + c_1 \geq 0$. Furthermore, the particle bed represents an area reduction (i.e., $A_6 > A_1$). Following [18], two more area parameters A_T and A_S are defined as

$$A_T = A_1 \left| \frac{u_6}{c_6} \right| \left[\left(\frac{\gamma - 1}{\gamma + 1} \right) \left(\frac{u_6}{c_6} \right)^2 + \left(1 - \frac{\gamma - 1}{\gamma + 1} \right) \right]^{-\frac{1}{2\left(\frac{\gamma-1}{\gamma+1}\right)}}, \tag{13}$$

$$A_S = A_1 \left| \frac{{u_6}^0}{{c_6}^0} \right| \left[\left(\frac{\gamma - 1}{\gamma + 1} \right) \left(\frac{{u_6}^0}{{c_6}^0} \right)^2 + \left(1 - \frac{\gamma - 1}{\gamma + 1} \right) \right]^{-\frac{1}{2\left(\frac{\gamma-1}{\gamma+1}\right)}}, \tag{14}$$

where ${u_6}^0$ and ${c_6}^0$ are given by

$${u_6}^0 = \left(\frac{\gamma - 1}{\gamma + 1} \right) u_6 + \left(1 - \frac{\gamma - 1}{\gamma + 1} \right) \frac{(c_6)^2}{u_6}, \tag{15}$$

$$\left({c_6}^0\right)^2 = \left(c_6^2\right) \left[\left(1 + \frac{\gamma - 1}{\gamma + 1} \right) \left(\frac{u_6}{c_6} \right) - \left(\frac{\gamma - 1}{\gamma + 1} \right) \left(\frac{c_6}{u_6} \right) \right] \left[\left(\frac{\gamma - 1}{\gamma + 1} \right) \left(\frac{u_6}{c_6} \right) + \left(1 - \frac{\gamma - 1}{\gamma + 1} \right) \left(\frac{c_6}{u_6} \right) \right]. \tag{16}$$

For our initial conditions, the values of A_T and A_S are computed, and we note that $A_6 > A_S > A_T > A_1$. Based on this ordering, we classify the L-M wave structure as belonging to case VI and correspondingly the R-M wave structure as belonging to case II, according to the classification of [18]. The resulting resonant wave structure that is most relevant for our setup is given in Fig. 4(b). Immediately following the arrival of the incident shock at the sudden area reduction, there is a reflected shock wave moving to the left, a stationary wave at $x = 0$ across which the area sees a reduction, followed by a resonant expansion fan whose head is attached to the stationary wave while its tail moves to the right, followed by a contact discontinuity that also travels to the right, and finally a right moving transmitted shock.

The wave structure described in Fig. 4(b) is illustrated with approximate relative positions of different wave components in a duct with sudden area reduction in Fig 4(c). State ⑥ represents the post-shock flow ahead of the reflected shock moving to the right and the Mach number of the reflected shock will be denoted by M_r. State ⑤ represents the subsonic side of the reflected shock, and the flow continues to travel in the positive streamwise direction. Between states ⑤ and ④ there is a sudden area change where the incoming subsonic flow expands isotropically, and this is the stationary wave mentioned previously. At state ④ there is a resonant expansion wave which is coincident with the stationary wave. The upstream front of the expansion fan is stationary, while the downstream front is moving into region whose state is given by ③. States ③ and ② are connected by a contact discontinuity across which the density and temperature change. The ambient state ① and state ② are connected by the transmitted shock, which is traveling in the positive streamwise direction and whose Mach number is denoted by M_t.

We now describe the step-by-step process involved in obtaining the unique solution represented by the wave structure given in Fig. 4(c). We consider a representative example with incident shock Mach number 3.0 and an area change of 10% across the particle bed.

Step 1 - We are given the post-shock state ⑥, from which for varying values of the reflected shock Mach number M_r we obtain the shock speed and the flow quantities across the reflected shock for state ⑤. We now demand that (i) the velocity of the reflected shock u_r be negative; i.e., that the reflected shock must move upstream, and (ii) the gas velocity of state ⑤ be positive. These constraints restrict the possible reflected shock Mach numbers to be between 1.3580 and 2.1040. For all the possible values of the reflected shock Mach number, the flow for state ⑤ is always subsonic.

Step 2 - The next is to match the post-reflected-shock state ⑤ with the stationary wave, which is isentropic flow through an area change, to obtain the flow state ④. In our case the area change is like a contracting nozzle, since $(A_6 = A_5) > (A_4 = A_1)$. A subsonic inflow into a contracting nozzle can at most reach a sonic state. In the present work we consider area reductions of 10% to 25%, and in all these cases the flow becomes sonic for state ④. This is indeed a condition for resonance, since only then the head of the expansion fan that is to follow, whose velocity with respect to the local flow must be sonic, will remain stationary in the laboratory frame, and coincide with the stationary wave. For smaller area reductions it is possible that the flow at state ④ may still be subsonic and deviate from the scenario shown in Fig. 4(c). However, if the flow reaches a sonic state after the area reduction, there is only one unique possible solution for the reflected shock and the post-reflected-shock flow. For example, for an area change of 10%, the flow must enter the area reduction at a Mach number of 0.6787 to reach the sonic condition (or Mach 1.0) as it exits the area reduction. The corresponding reflected shock Mach number is 1.4180 with a slow upstream velocity of $u_r = -33.87$ (m/s). Table III summarizes the flow properties for states ⑤ and ④.

Step 3 - The resonant wave is an expansion fan whose upstream front is stationary and the downstream front is moving at local speed of sound into a region with state ③. The expansion fan is an isentropic process and flow properties within the expansion fan can be easily evaluated in terms of the Mach number corresponding to state ③. In particular, we calculate the gas velocity and pressure for state ③ for varying values of M_3 and plot them in Fig. 5 as the black curve.

Step 4 - We know that the flow with state ③ is followed by a contact discontinuity to state ② and a transmitted shock from state ② to ①. Since the pressure and velocity do not change across a contact discontinuity, the pressure and velocity behind the transmitted shock for state ② must match those presented in Fig. 5 for state ③. Since the ambient conditions at ① are known, the state of the gas behind the transmitted shock can be fully expressed in terms of the transmitted shock Mach number, M_t. We vary the transmitted shock number and plot in Fig. 5 the resulting pressure versus velocity for state ② as the red curve. It is clear from the plots that there is a unique solution given by the intersection point between the two curves, which yields a common pressure and velocity for states ③ and ②. We find that the transmitted shock Mach number to be nearly the same as that of the incident shock (i.e., $M_t \approx 3$) with a velocity of $u_t = 1029.414(m/s)$.

Step 5 - The corresponding densities for states ③ and ② however are not be equal. This results in a contact discontinuity across which both density and temperature change. The contact discontinuity travels downstream at the local gas velocity. In the case of 10% volume reduction the density jump across the contact discontinuity is 1.0137. Table III summarizes the flow properties for states ③ and ②. Strength of the contact discontinuity is computed by taking the ratio of densities in state 3 and 2, which is presented in Table III.

We repeat Steps 1-5 for different area changes to obtain the flow properties across the wave structure. Plots of pressure, density, and velocity for different area changes are presented in Fig. 6. In addition, the key properties of these solutions are listed in Table IV. These baseline Rie-

mann solutions of the sudden contraction will be used to compare with those from the numerical simulations of shock propagation through a random particle bed to be presented in the subsequent sections.

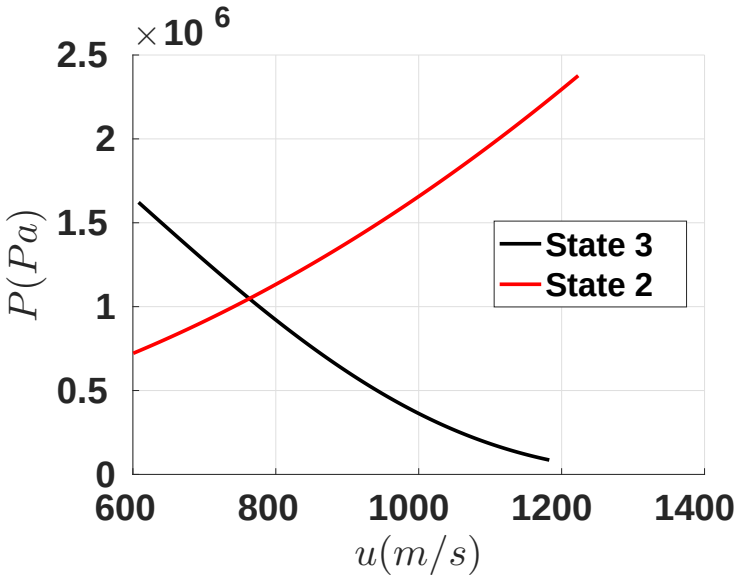

FIG. 5: Plot of pressure as a function of velocity for different Mach numbers for states three and two.

TABLE III: Flow properties across the domain for 10% area reduction and for an imposed shock Mach number of 3.

Flow property	State 6	State 5	State 4	State 3	State 2	State 1
$u(m/s)$	762.5293	428.9251	602.9424	763.3319	763.3319	0
$P(MPa)$	1.047025	2.281653	1.640794	1.046600	1.046600	0.101325
$\rho(kg/m^3)$	4.6470	7.9967	6.3187	4.5829	4.6459	1.2048
M	1.3577	0.6787	1.0	1.3500	1.3576	0

4 Simulation Results

In this section we present numerical results of a shock propagating over a random bed of particles that are held fixed in space and time. We study the effect of volume fraction for a fixed shock Mach number $M_s = 3$. We compute the individual force histories on each particle as well as flow field information to extract data about the behavior of the shockwave as it propagates through the random particle bed. The main insights that can be obtained from the results are an understanding of how the interaction of a shock with the distribution of particles affects its propagation, as well as how the presence of a large number of adjacent particles modifies the force experienced by each individual particle as it interacts with the shock wave.

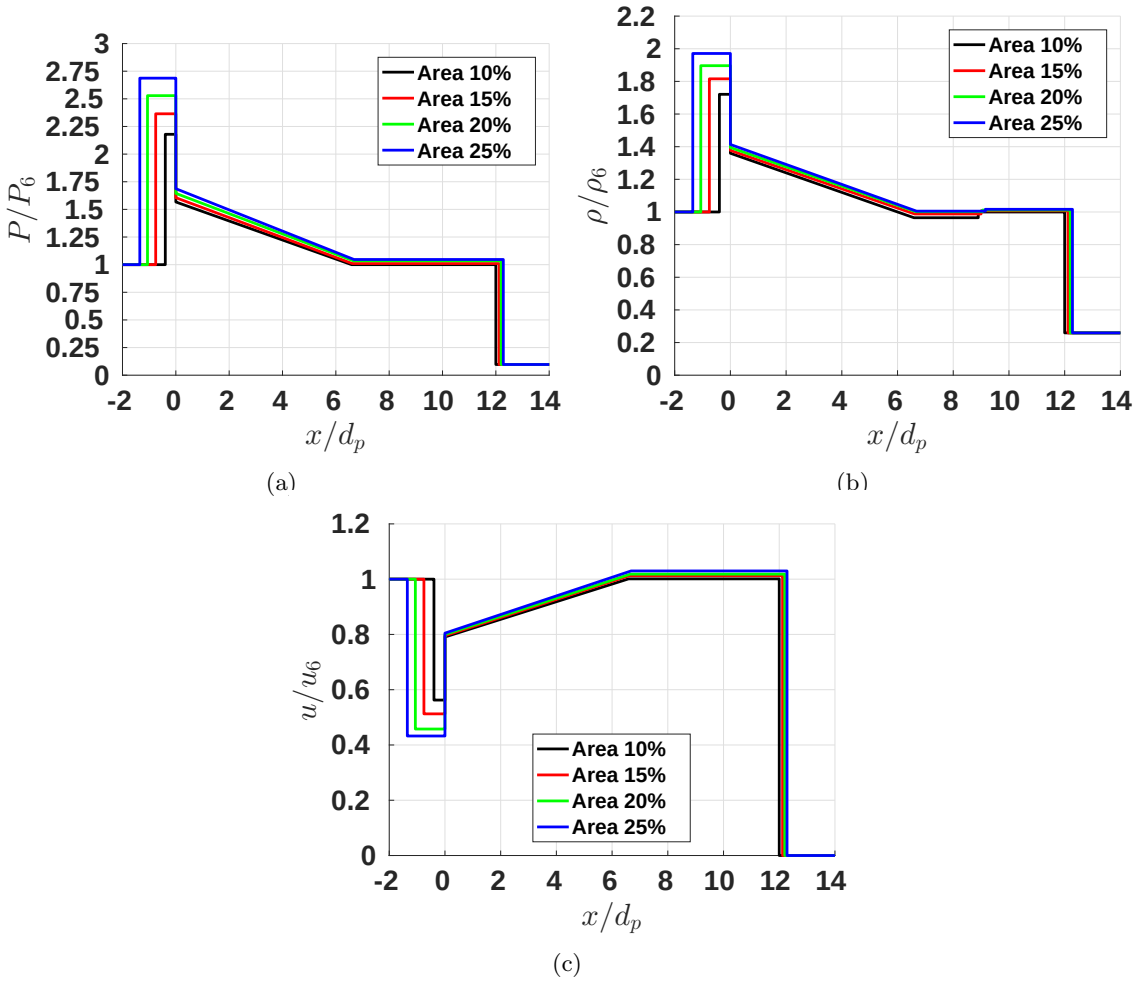

FIG. 6: Plot of normalized (a) pressure, (b) density, and (c) velocity across the domain at $t/\tau = 12$ for $\phi_1 = 10\%, 15\%, 20\%, and 25\%$.

TABLE IV: Flow properties across the domain for different area reductions and for an imposed shock Mach number of 3.

ϕ_1	M_r	$u_r(m/s)$	M_t	P_5/P_6	ρ_5/ρ_6	u_5/u_6	P_4/P_6	ρ_4/ρ_6	u_4/u_6	P_2/P_6	ρ_2/ρ_6	u_2/u_6	ρ_2/ρ_3
10%	1.41	-33	3.00	2.178	1.721	0.562	1.567	1.359	0.791	1.000	1.000	1.000	1.014
15%	1.47	-64	3.03	2.365	1.816	0.513	1.606	1.377	0.795	1.020	1.007	1.012	1.019
20%	1.52	-91	3.05	2.529	1.896	0.471	1.645	1.395	0.799	1.035	1.012	1.021	1.009
25%	1.56	-115	3.07	2.687	1.971	0.432	1.687	1.414	0.805	1.047	1.016	1.029	1.011

4.1 Streamwise Force on the Particles

The time histories of streamwise force for an imposed shock propagating through a three-dimensional random bed of particles are presented in Fig. 7 for the four different volume fractions considered in this study. Note that the streamwise force history for each particle is shown in the figure; since each bed contains hundreds of particles, there are hundreds of curves. The force plots are affectionately referred to as "force spaghetti" plots because of the chaotic and tangled appearance of the drag force histories. The time resolved force histories of each particle paint a picture of the flow field that every particle sees during the shockwave interaction.

In a sense each time history of force shown in Fig. 7 qualitatively resembles that shown in Fig. 3. This includes the characteristic feature of a rapid rise in the streamwise force due to the primary shock, whose arrival time depends on the streamwise location of the particle, and manifests as the horizontal shift seen in the different force histories. In Fig. 7 we note that the peak drag coefficients of the leading particles in the random bed correspond to the limit of the shock interaction with a single isolated particle case. The leading particles are almost isolated in the limit of small shock interaction times; i.e., at times before transverse reflections from neighboring particles arrive to disrupt the single particle behavior. In the classical single shock-particle interaction case, the drag coefficient will quickly rise as the shock passes over the particle and then the drag coefficient will either drop to zero for a subcritical inviscid case or to a constant non-zero value for the supercritical case. For the supercritical case, the post-shock velocity is supersonic, and a bow shock forms upstream of the particle, causing the wave drag to be non-zero. Thus, as a result of interaction with the primary shock front, each force history rapidly reaches a peak and decays over time.

However, substantial differences are seen between the different force histories, emphasizing the important role of secondary interactions with the reflected waves and wakes of the other particles in the domain. For example, we can see that there are negative drag coefficients for some of the particles in the bed, indicating that the pressure behind the particle is larger than the pressure in front of it. In comparison, for an isolated particle subjected to a Mach 3 shock wave, at all later times the drag coefficient remains larger than unity due to the formation of a bow shock ahead of the particle. The presence of large variations in the streamwise force, including negative force values, indicate the strong influence of neighbors on the force history experienced by the different particles. Hence in what follows we will quantify both the mean force within the particle bed as well as the particle-to-particle force variation seen within the bed.

One way to simplify the characterization of the complex force histories seen in Fig. 7 is to focus only of the peak values of C_D for each particle. Fig. 8 plots the peak streamwise drag coefficient, $C_{D,peak}$, as a function of nondimensional streamwise distance x/d_p of the particle center for the same four volume fractions shown in Fig. 7. It is clear from the figure that there is a downward trend in the peak drag, that there is stochastic variation, and that the rate of decrease in the peak drag increases as the volume fraction increases. For each volume fraction, a least squares linear fit for the peak drag is carried out. The linear fit is plotted as the red line in the figure, and is given by $\langle C_{D,peak} \rangle = p_1 \xi/d_p + p_2$, where ξ is measured from the leading edge of the particle bed. Here p_1 is the slope of the line and can be thought of as the rate of decrease of peak drag, and p_2 is the intercept at $\xi/d_p = 0$, or the mean peak drag experienced by the leading particles. For the four different volume fractions Table V presents p_1 and p_2 along with the goodness of the fit measured in terms of the R^2 value and also the rms value (σ) of the deviation of the actual peak C_D about the fit. Since $\langle C_{D,peak} \rangle$ is typically in the range 0.8 to 1.6, the value of σ suggests more than 20% particle-to-particle variation in the peak drag coefficient.

For comparison, also plotted in Figs. 8(a) and 8(c) are the peak drag coefficients obtained in the case of Mach 3 shock propagation over a FCC array of particles at 10% and 20% volume fractions.

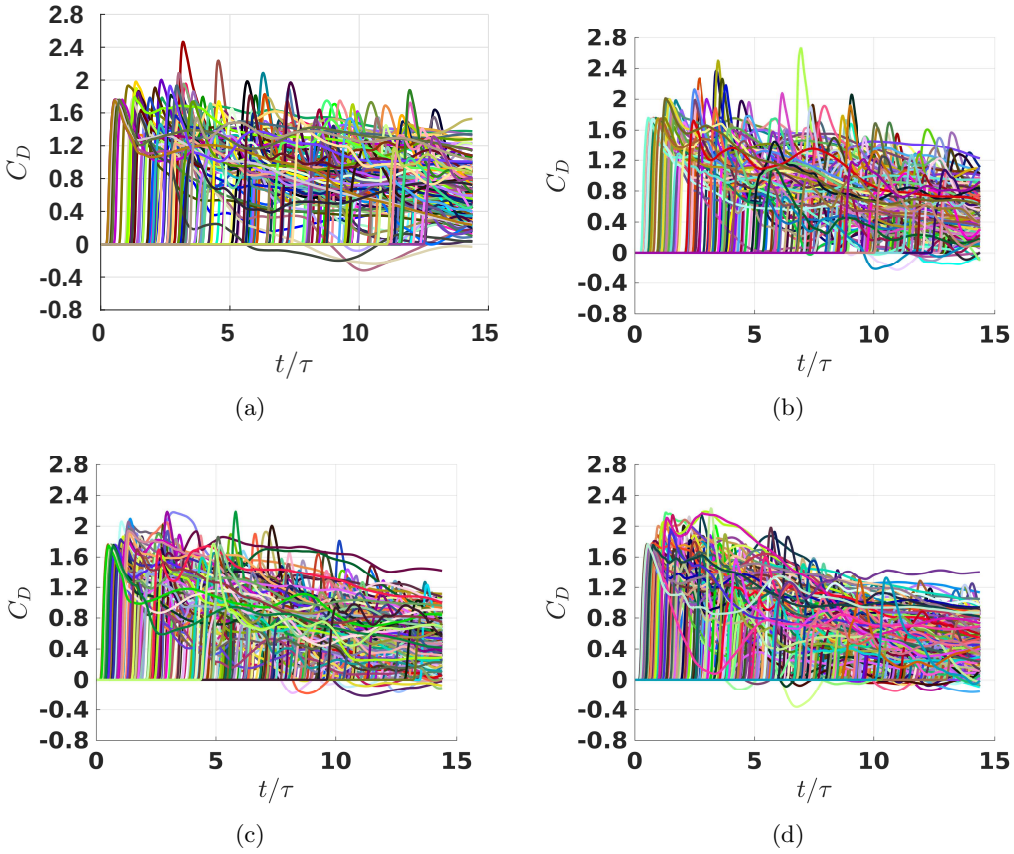

FIG. 7: Plot of streamwise drag coefficient, C_D, as a function of nondimensional time t/τ and for volume fractions of (a) $\phi_1 = 10\%$, (b) $\phi_1 = 15\%$, (c) $\phi_1 = 20\%$, and (d) $\phi_1 = 25\%$.

The figure clarifies the importance of particle arrangement. The results for the FCC arrangement are for five streamwise planes of particle [15] which are shown in the figure. By symmetry all particles within a streamwise plane of FCC array experience the same stream-wise drag force. For both volume fractions the drag coefficient of the FCC arrangement increased from the leading (first) plane of particles to the third plane, and then slightly decreased towards the fifth plane of particles. Three mechanisms were identified contributing to the downstream variation of peak drag force: (i) As the primary shock transmits through the particle bed, diffraction around each plane of particles can lead to regions of shock focusing in the wake and contribute to higher drag on the subsequent plane of particles. (ii) If the Mach number of the post shock flow is greater than critical value, shocklets from around the particles, which dissipate energy from the transmitted shock as it propagates into the bed. This dissipation contributes to the downstream weakening of the shock and hence reduction in the peak drag force. (iii) Further wave reflections from the neighboring particles contribute constructive and destructive interferences and corresponding modifications of the force. In the case of FCC arrangement, shock focusing effect dominates over the first few planes of particles. In the random array, the effect of shock focusing and constructive interference can be seen as the cause of above average peak force experienced by some of the particles. However, when averaged over all the particles at any streamwise location, we see that the effect of shock dissipation dominates and the mean peak force steadily decreases with downstream distance from the leading edge of the particle bed. Also, in the random array occasional particles are subjected to destructive interference and the resulting weaker shock contributes to substantially lower than mean drag.

Also plotted in Fig. 8 are the results for simple cubic (SC) array of particles at 10% and 20% volume fractions. In this case 10 planes of particles are considered in the streamwise direction and due to symmetry the drag force on all the particles that lie on a streamwise plane are the same. As can be expected, the peak drag force for the leading particle in the random, FCC and simple cubic array are the same. The peak drag force on the subsequent planes of SC are qualitatively similar to that of the FCC arrangement. In the case of SC arrangement, the peak drag increases from the first to the second plane, but steadily decreases from the third plane onwards. It is interesting to observe that the peak drag force in the structured arrays are substantially higher than the mean drag of the random array, thus emphasizing the importance of arrangement on promoting constructive interference. The streamwise decay of the peak drag force in the SC arrangement is about the same as that for the random array signifying similarities in their shocklet-induced dissipation.

ϕ_1 (%)	p_1	p_2	R^2	σ
10	-0.0385	1.7705	0.2354	0.2468
15	-0.0568	1.7767	0.3122	0.2934
20	-0.0745	1.7687	0.5249	0.2471
25	-0.0896	1.7562	0.6359	0.2391

TABLE V: Least-squares curve fit statistics for peak streamwise drag $C_{D,peak}$.

To gain some insight into the variations in peak drag observed in Figs. 7-8, we plot their corresponding histograms in Fig. 9 as a function of the scaled peak drag coefficient, $C_{D,peak} - \langle C_{D,peak} \rangle$. The histograms are obtained by sorting the peak drag coefficients into bins of equal width for each volume fraction. Also plotted as the red curve is a normal distribution that best fits the histogram. Note that at all the volume fractions, the distribution of the peak drag coefficient is reasonably close to a normal distribution. If one were to use point-particle drag models for the simulation of shock propagation through a random bed, it is not sufficient to capture the mean

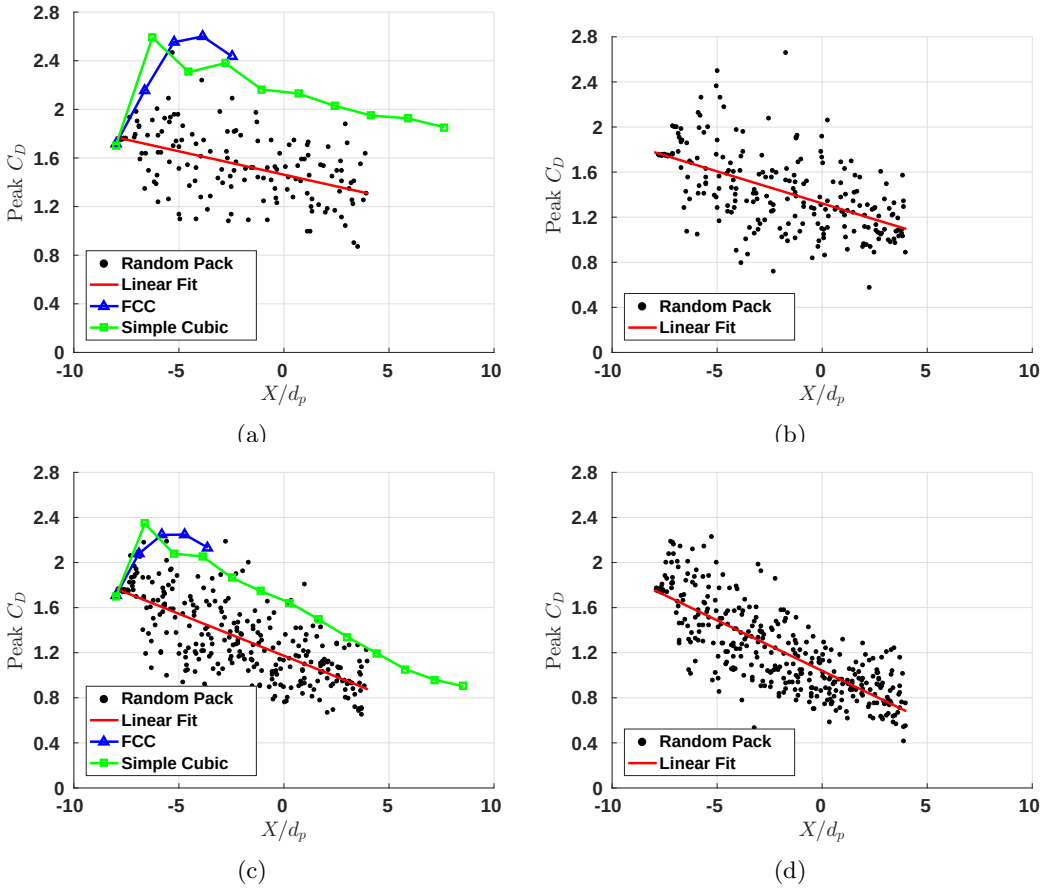

FIG. 8: Plot of peak streamwise drag coefficient, $C_{D,peak}$, as a function of distance x/d_p. The red curve is the least squares linear fit for the data, $\langle C_{D,peak} \rangle$. Here, (a) $\phi_1 = 10\%$, (b) $\phi_1 = 15\%$, (c) $\phi_1 = 20\%$, and (d) $\phi_1 = 25\%$.

drag force. As indicated in Figs. 7 and 8, the substantial particle-to-particle variation in the drag force must also be taken into accounted. Based on the near-Gaussian distribution, a stochastic model can be constructed to account for the distribution of drag histories about the mean.

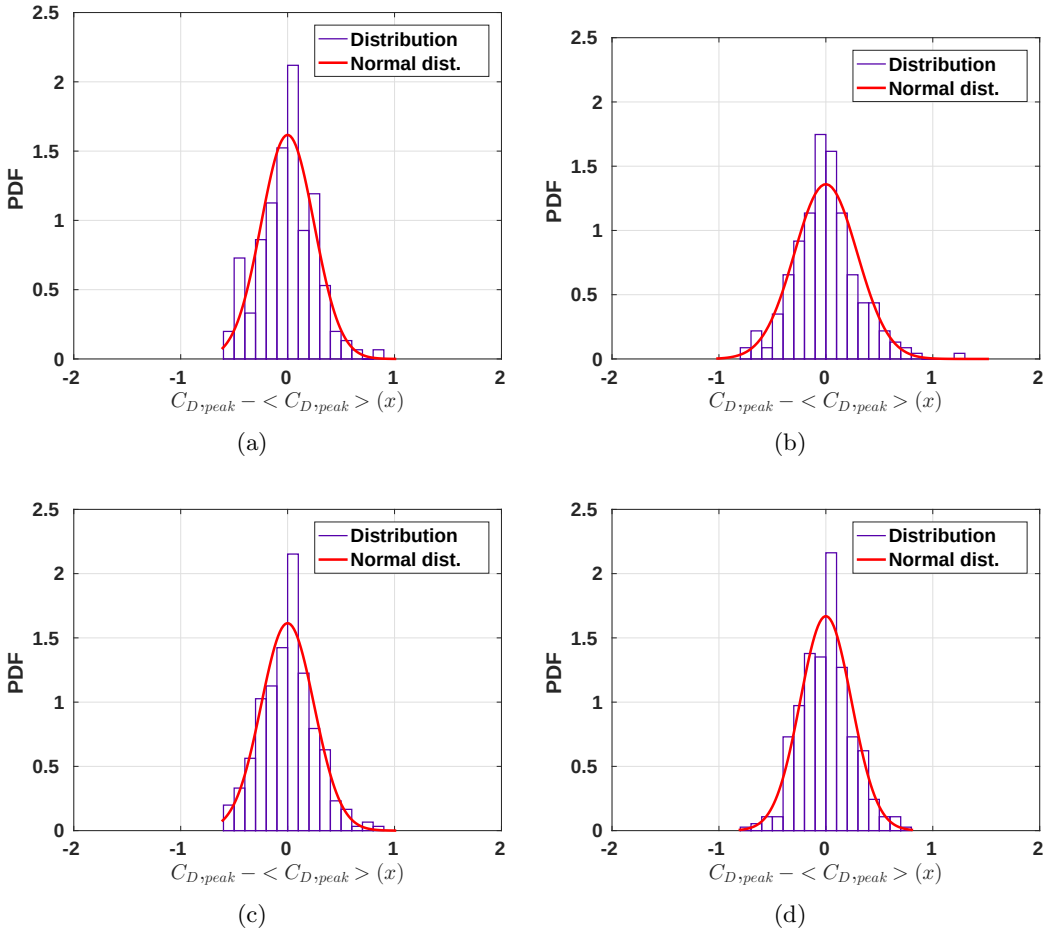

FIG. 9: Histogram of scaled peak drag coefficient, $C_{D,peak} - \langle C_{D,peak} \rangle$. The red curve is a normal distribution fit for the data given in Table V. Here, (a) $\phi_1 = 10\%$, (b) $\phi_1 = 15\%$, (c) $\phi_1 = 20\%$, and (d) $\phi_1 = 25\%$.

On a local level, if we define the undisturbed flow witnessed by each sphere to be the flow in its absence, but in the presence of all other spheres, the local undisturbed shock propagating past each particle will depend on the precise relative arrangement of all its upstream neighbors. The unique neighborhood of each particle results in a unique undisturbed flow seen by this particle, which then contributes to its departure from the mean drag and lift forces. First, we will consider the local volume fraction of each particle, obtained in terms of its Voronoi volume, to provide an overall measure of its neighborhood. A particle with a small Voronoi volume is closely surrounded by its neighbors, while a particle with a large Voronoi volume has its neighbors far away. Here we will investigate the correlation of the peak drag coefficient experienced by a particle with its local volume fraction. A positive correlation can be expected, since a higher local volume fraction would indicate higher velocity and a faster propagation of the shock resulting in a higher drag.

In Fig. 10 we plot the normalized variation in peak streamwise drag coefficient as a function of scaled local volume fraction. The normalized variation in peak drag coefficient is defined by

$(C_{D,peak} - \langle C_{D,peak}\rangle)/\langle C_{D,peak}\rangle$, where $C_{D,peak}$ is the peak drag coefficient for each particle and $\langle C_{D,peak}\rangle$ is the mean value shown by the red line in Fig. 8. The scaled local volume fraction is given by, $(\phi_i - \phi_1)/\phi_1$. From the figure we see that increasing the global volume fraction from 10% to 25% decreases the spread in the local volume fraction, which is consistent with the statistics provided in Table I. However, with increasing global volume fraction, the spread in the fluctuating peak streamwise drag coefficient slightly increases. Contrary to expectation, this figure shows that the increase (or decrease) in the peak drag coefficient does not correlate with an increase (or decrease) in the local volume fraction. This observation is consistent with findings of Akiki *et al.* [29] who also noted that in the case of a uniform steady flow over a random bed of particles, the deviation of the drag force on each particle from the bed-averaged mean does not correlate with the local volume fraction. In fact, other definitions of local volume fraction, such as number of particles within a large volume (Quintanilla & Torquato [30]) or distance to the n-nearest neighbor (Yazdchi et al. [31], Matsumura and Jackson [32]), can be used instead of the present definition based on local Voronoi volume. Nevertheless, local volume fraction as defined with all such isotropic definitions do not explain the particle-to-particle variation in the drag force [29].

It is clear that two different particles with the same local volume fraction can have vastly different peak drag forces. For example, the two particles marked **A** and **B** in Fig. 10(b) have nearly the same local volume fraction, but their peak C_D are respectively 1.9194 and 0.7251. The particle marked **A** experiences a peak drag force 45% higher than the mean, while the particle marked **B** experiences a peak drag force 50% lower than the mean. The neighborhood and the resulting pressure field around the two particles as the shock propagates through the neighborhood of the two particles are shown in Fig. 11. It is clear that particle **B** is sheltered by another particle that is located directly upstream close to it, thus decreasing the local strength of the shock encountering particle **B**. Whereas, particle **A**'s neighbors are located such that they help in focusing the transmitted shock as it encounters particle **A**. In both these cases the shock strength can be estimated from the pressure contours. Thus, local volume fraction, or local Voronoi volume of a particle, is not an adequate measure [29, 33]. A more precise knowledge of where the neighboring particles (especially upstream neighbors) are located is critical in explaining higher or lower than mean drag forces experienced by the different particles within the bed [34, 35]. Anisotropic measures of local neighborhood involving distances to the nearest neighbors along the upstream, downstream and lateral directions were introduced by Akiki *et al.* [29, 33], and these measures were shown to better correlate with the drag force experienced by the different particles.

We now investigate the time history of the mean drag force. In order to avoid the influence of the downstream shock decay, we will calculate the mean drag force over bins of particles. We define each bin to be two diameters wide along the streamwise direction. Thus, the first bin will include all particles whose center lies within $-8 \leq x/d_p < -6$, and correspondingly other bins are defined. The force histories for particles in the first, third and fifth bin for $\phi_1 = 10\%$ are plotted in Fig. 12(a-c). It can be seen that the shock strength within each bin can be taken to be nearly uniform. The time history of C_D presented in Fig. 12(a-c) for all the particles within the bin are sifted in time and averaged. The bin-averaged C_D for bin-1 is shown in Fig. 12 (d). Also plotted in the figure is one sigma variation, along with drag history of a sample particle. It can be observed that the level of particle-to-particle variation seen in the peak value of C_d persists over the entire duration of the simulation. However, as can be seen in the figure, there is no guarantee that the particle with the higher peak will continue to experience higher than mean force. This is due to the fact that the neighborhood configuration that was responsible for shock focusing and increased peak force may not present favorable conditions for increased drag during post-shock flow. Finally, Fig. 12(e) shows the time history of the bin-averaged force for 15% volume fraction for bin-1, bin-3 and bin-5, along with the time history of force for an isolated particle subjected to Mach 3 shock.

Note from the figure that the drag coefficient for a single particle is larger than for those for bins 1, 3, and 5, and that the peak and short time transient downstream behavior decreases monotonically as the bin number increases.

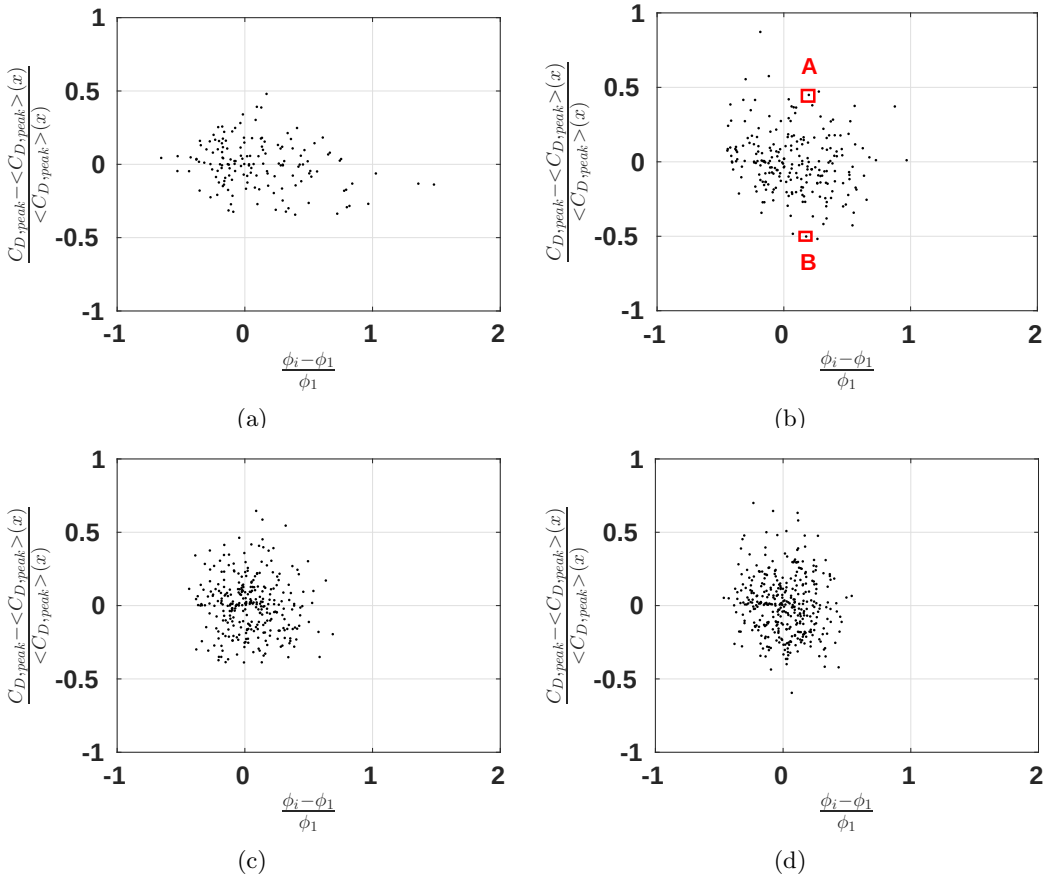

FIG. 10: Plot of normalized peak streamwise drag coefficient, $(C_{D,peak} - \langle C_{D,peak}\rangle)/\langle C_{D,peak}\rangle$, as a function of scaled local volume fraction (Voronoi volume), $(\phi_i - \phi_1)/\phi_1$, for (a) $\phi_1 = 10\%$; (b) $\phi_1 = 15\%$; (c) $\phi_1 = 20\%$; and (d) $\phi_1 = 25\%$.

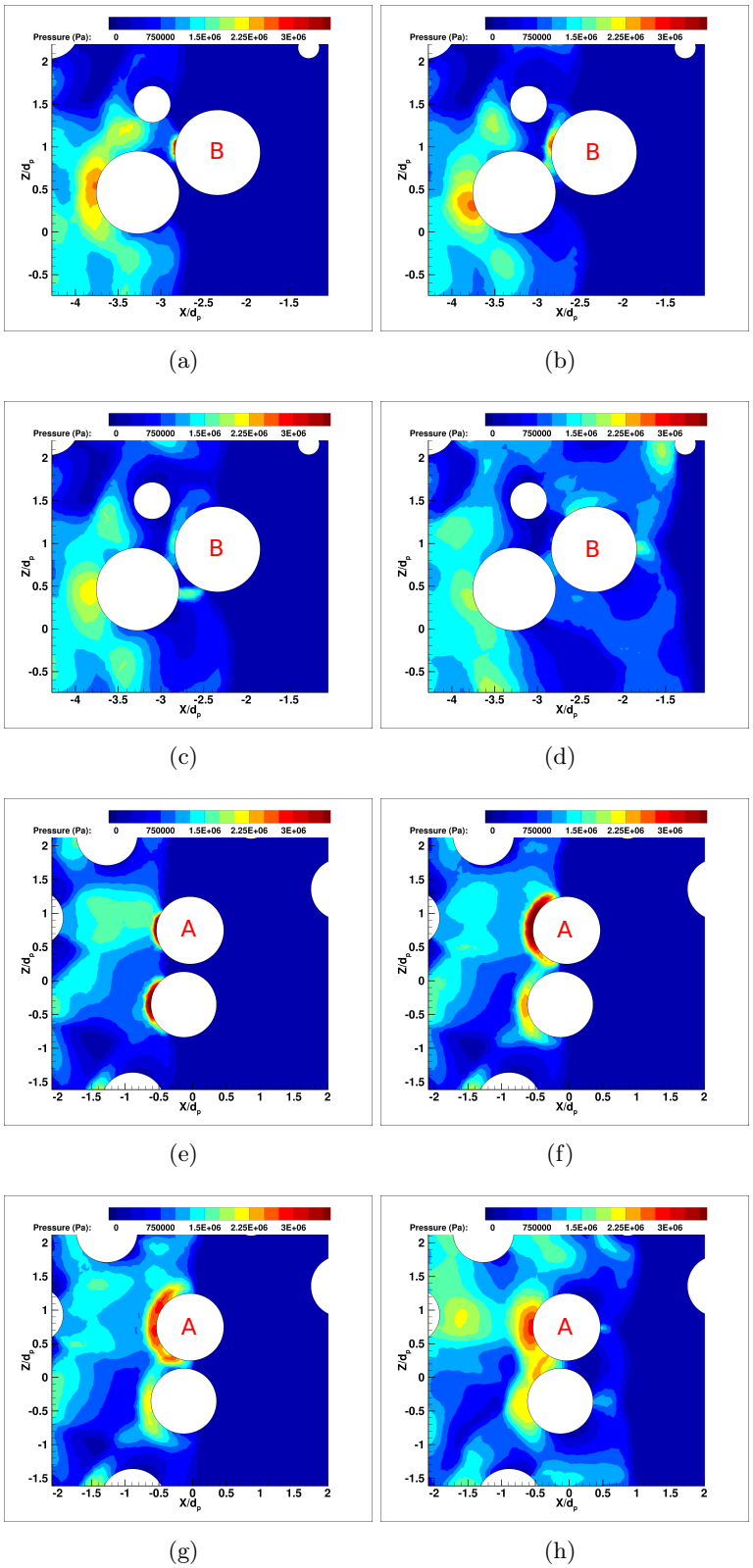

FIG. 11: Contour plot of pressure for (a-d) particle with low force (particle B form Fig. 10b) and (e-h) particle with high force (particle A form Fig. 10b) along the x-z plane at four different t/τ as the transmitted shock passes over the particles.

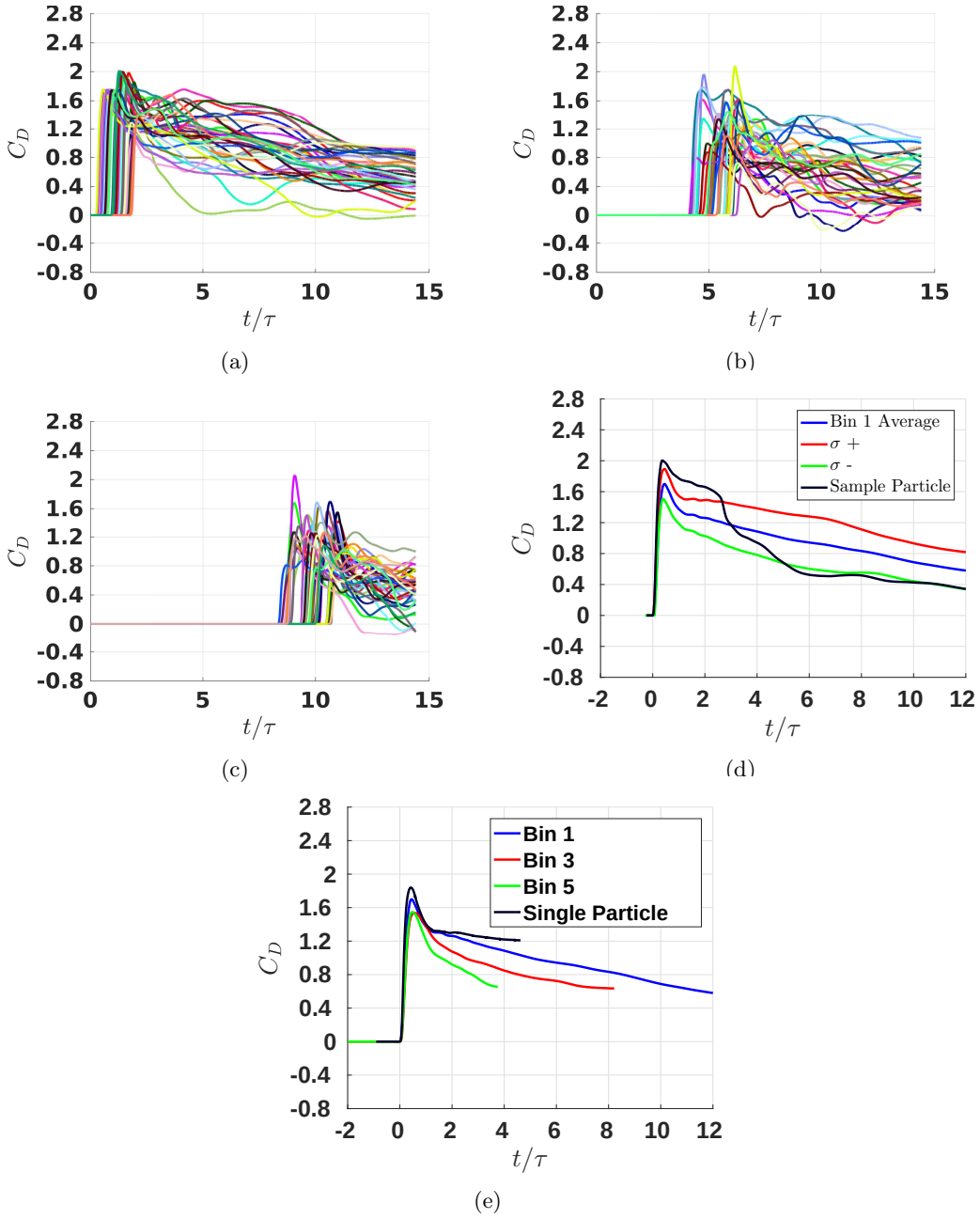

FIG. 12: Plot of streamwise drag coefficient, C_D, as a function of nondimensional time t/τ and for volume fraction $\phi_1 = 15\%$ for (a) bin 1 : $-8 < x/d_p < -6$, (b) bin 3 : $-4 < x/d_p < -2$, and (c) bin 5 : $0 < x/d_p < 2$. (d) Force averaged over bin 1 along with one sigma variation and force on a sample particle. (e) bin 1, bin 3, bin 5 averaged along with force on a single particle.

4.2 Transverse Particle Forces

We plot in Fig. 13 the spaghetti plot of y-force on all the particles for 10-25% volume fraction. The results for force in the z-direction show similar behavior and are not shown here. From the plot we see that the mean transverse force, averaged over all the particles over time is zero, but that there are significant variations. Fig. 14 also shows the time history of net transverse force magnitude (vector sum of y and z forces). As with the drag force, the transverse force coefficient is identically zero until the arrival of the transmitted shock. However, the transverse force due to the transmitted shock is significant only in situations where the shock is substantially oblique when it encounters the particle. In most other cases, the transverse force is due to the supercritical and unsteady nature of the post shock flow. Thus, not only the magnitude, but also the instance when the transverse force reaches a peak, varies strongly from particle to particle. It is also important to note that the transverse force can be 20 to 40% of the streamwise force. Macroscale simulations of shock interaction with a point particle model typically accounts for only the streamwise force on the particle bed. Even though the mean transverse force is zero, the strong instantaneous transverse force on the different particles is likely to play a role in both the shock transmission and the long term motion of the bed of particles.

Fig. 15 plots the peak values $C_{L,peak}$ for the different particles as a function of their streamwise location. The linear curve shown in Fig. 15 is given by $\langle C_{L,peak} \rangle = q_1 \xi / d_p + q_2$, with the statistics of the least squares fit given in Table VI. The slow decay of the peak transverse force along the streamwise direction is due to dissipation-induced shock weakening. The variability in the peak lift force is of the same magnitude as the variability in the drag force. However, since the mean transverse force is smaller, the relative importance of transverse force variability increases. The histograms of the transverse force variation is presented in Fig. 16. By definition $C_{L,peak}$ is non-negative and as a result the peak transverse force is positively skewed. The variations in peak transverse force is compared to a log-normal distribution in Fig. 16.

ϕ_1 (%)	q_1	q_2	R^2	σ
10	-0.0046	0.4065	0.0176	0.1221
15	-0.0036	0.4291	0.0112	0.1191
20	-0.0154	0.4905	0.1770	0.1159
25	-0.0229	0.5363	0.3529	0.1096

TABLE VI: Least-squares curve fit statistics for total transverse drag $C_{L,peak}$.

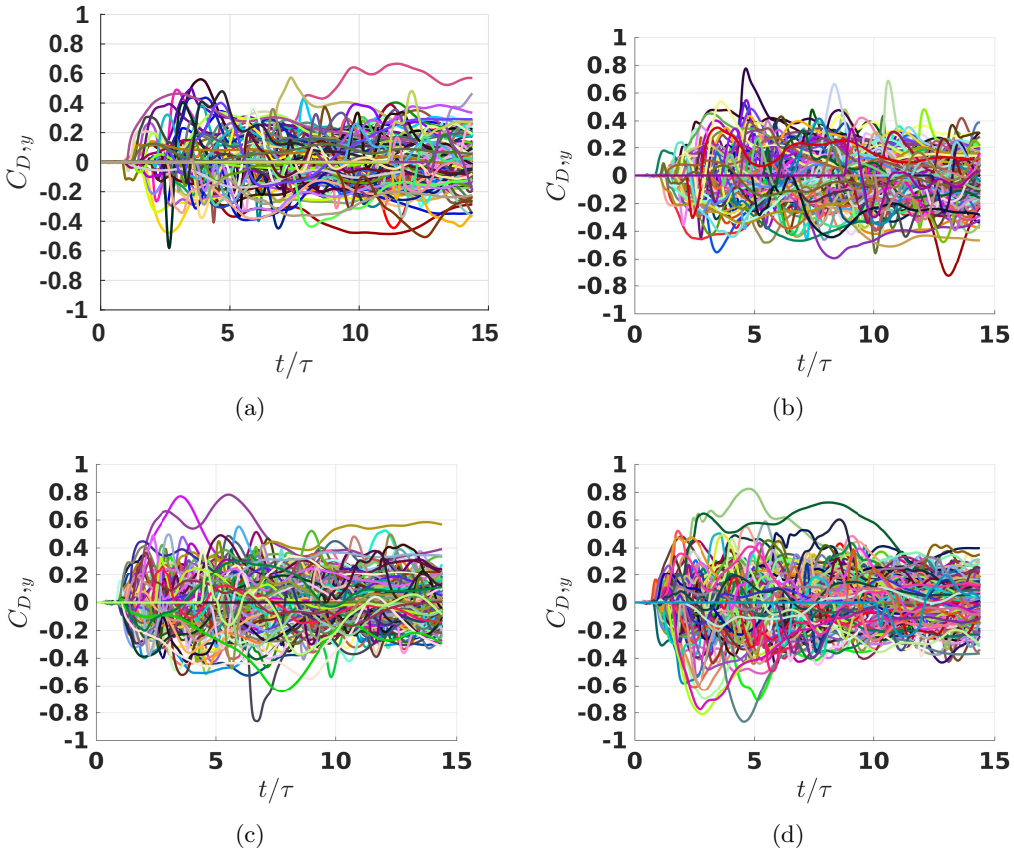

FIG. 13: (a) Plot of transverse drag coefficient, $C_{D,y}$, as a function of non-dimensional time t/τ and for volume fractions of (a) $\phi_1 = 10\%$; (b) $\phi_1 = 15\%$; (c) $\phi_1 = 20\%$; and (d) $\phi_1 = 25\%$.

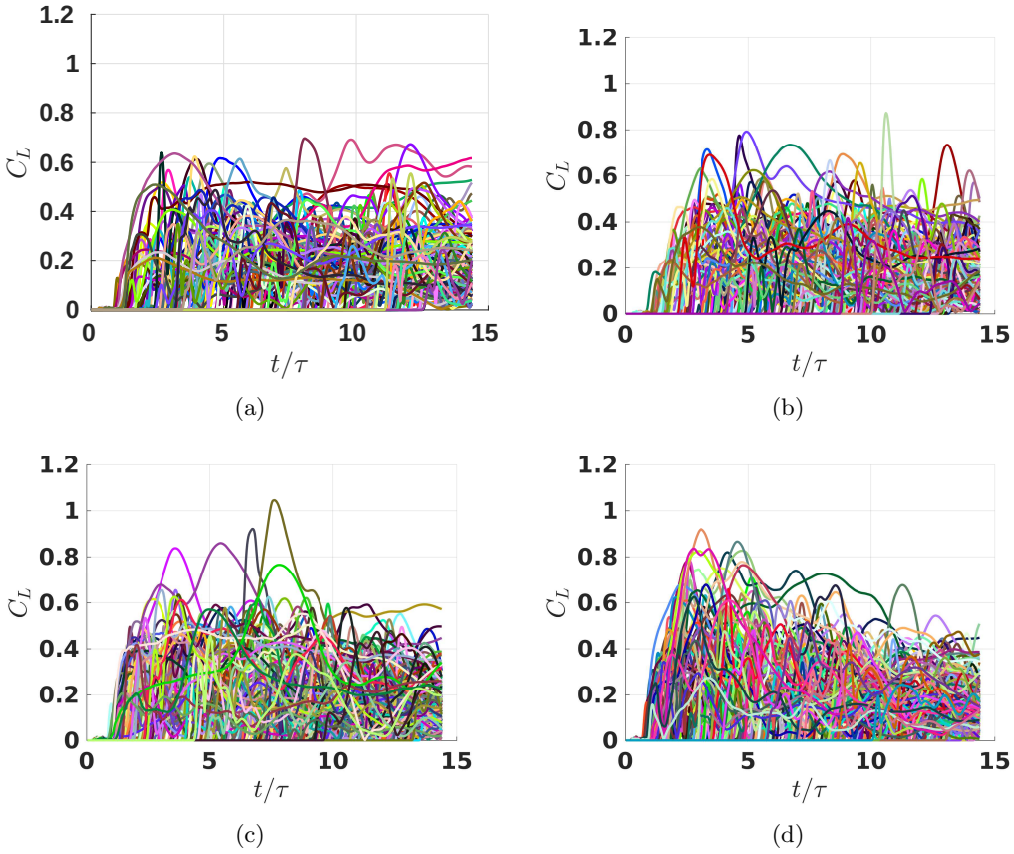

FIG. 14: (a) Plot of total transverse drag coefficient, C_L, as a function of non-dimensional time t/τ and for volume fractions of (a) $\phi_1 = 10\%$; (b) $\phi_1 = 15\%$; (c) $\phi_1 = 20\%$; and (d) $\phi_1 = 25\%$.

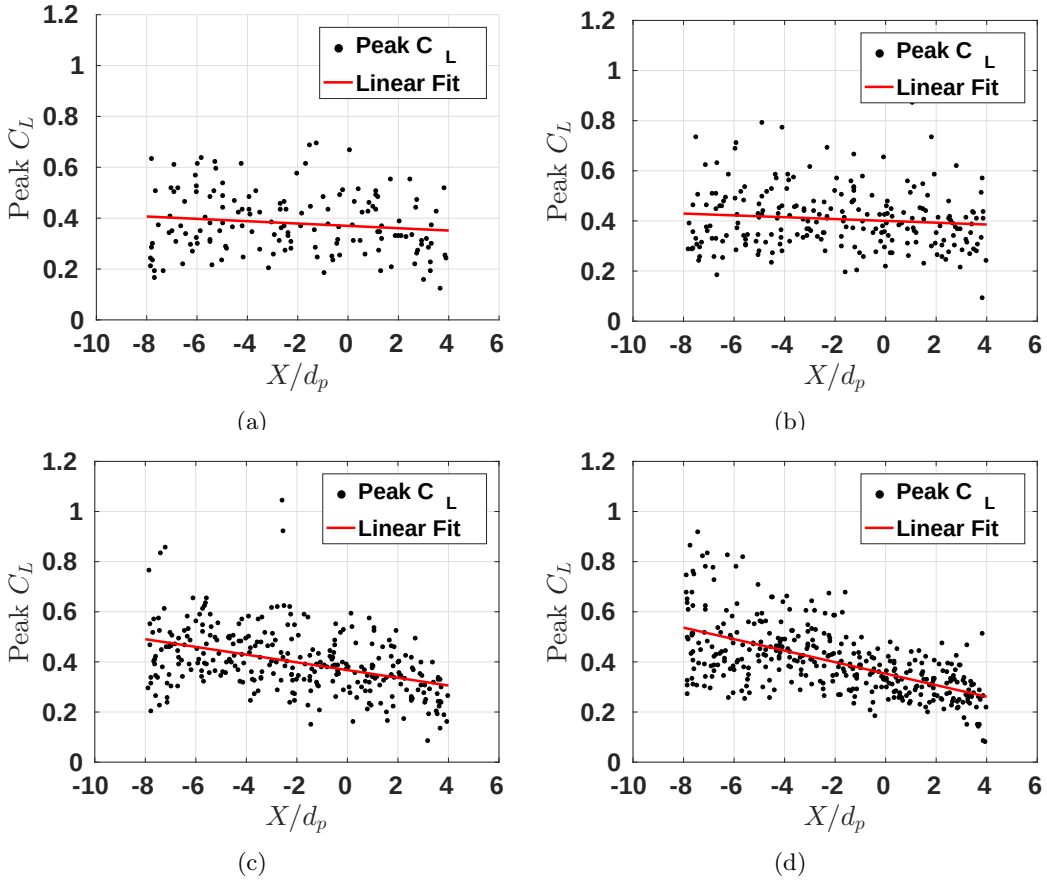

FIG. 15: Plot of peak total transverse drag coefficient, $C_{L,peak}$, for each particle. The red curve is the least squares linear fit for the data. Here, (a) $\phi_1 = 10\%$; (b) $\phi_1 = 15\%$; (c) $\phi_1 = 20\%$; and (d) $\phi_1 = 25\%$.

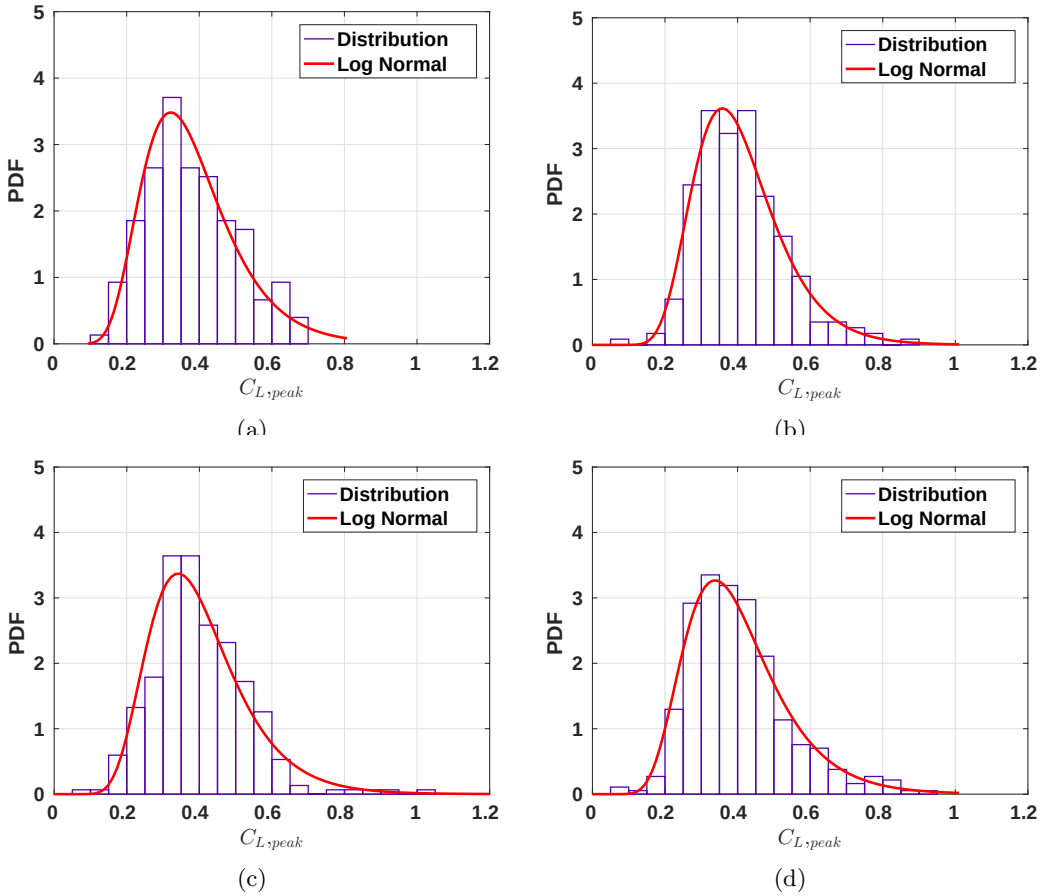

FIG. 16: Histogram of peak transverse drag coefficient, $C_{L,peak}$. The red curve is the Log-normal distribution fit for the data given in Table VI. Here, (a) $\phi_1 = 10\%$, (b) $\phi_1 = 15\%$, (c) $\phi_1 = 20\%$, and (d) $\phi_1 = 25\%$.

4.3 Flow Fields

To highlight the flow dynamics as the shock propagates through a random pack of particles, we show in Figs. 17-18 contour plots of the local Mach number, pressure, and vorticity magnitude on the $x-z$ plane at a fixed transverse ($y=0$) location in the middle of the computational domain. The particles cut by this $x-z$ plane are marked as white circles. Fig. 17 plots contours at four different times and for a volume fraction of $\phi_1 = 15\%$. The initial configuration and location of the imposed shock are shown in Fig. 17(a). As time proceeds, the imposed shock propagates downstream until it reaches the front of the particle bed. At later times a transmitted shock proceeds through the particle bed, which is visible in Mach number contours shown in Fig. 17(b). At this early time bow shocks can be seen to form ahead of the lead particles. A bow shock around an individual particle is expected to reach a steady stand-off distance from the particle, with the stand-off distance scaling as the size of the particle. In the case of a finite cluster of particles, a reflected shock forms from the coalescence of individual bow shocks. The reflected shock will propagate upstream to form a collective bow shock of the particle cluster [14, 34], whose stand-off distance from the cluster will scale as the lateral size of the cluster. In the present simulations the particle bed is of infinite extent in the lateral directions, due to the symmetry boundary conditions along the y and z directions. Based on this we can expect the reflected shock to continue to move upstream and reach a constant propagation velocity, in agreement with the Riemann solution of the corresponding nozzle flow. The imposed incoming shock is strictly planar and the reflected shock is nearly planar once the bow shocks of the different lead particles coalesce into one. In contrast, the transmitted shock is corrugated as it propagates through the particle bed. But it can be observed that the length scale of these corrugations is smaller than the particle diameter. Thus, shock arrival time in a porous medium can be reasonably well approximated to be that of a planar shock.

After the passage of the transmitted shock, shocklets are seen to form around the particles, which can be identified as regions of higher Mach number in Figs. 17(f-h). The existence of these shocklets is a direct consequence of the flow being supercritical; i.e., the post-shock Mach number is locally greater than one. This observation is consistent with previous findings of a shock propagating through a face-centered cubic array [15]. We note that the shocklets appear to connect nearest neighbors as the volume fraction increases beyond the dilute limit. In the pressure contours plots substantial variation in the pressure distribution around particles that are at roughly the same streamwise location can be observed. Such differences in pressure distribution directly contribute to particle-to-particle variation in the streamwise and transverse drag forces. In interpreting these figures it must be borne in mind that only a $x-z$ plane is shown. Nearby particles that do not cut this $x-z$ plane are not shown. However, such particles will have a strong influence on what is shown in these figures. As the primary shock weakens the pressure drop across the propagating primary shock decreases. However, due to shock reflection the pressure is high in the region between the reflected shock and the upstream particle front. Also due to internal compressional waves and their constructive superposition regions of high pressure can be seen within the particle bed, typically close to and upstream of the particles.

Since the simulations are inviscid, the vorticity (magnitude) shown in Figs. 17(j-l) is baroclinic in origin. In a viscous simulation additional vorticity will be generated on the surface of the sphere due to no-slip boundary condition. Nevertheless, it is interesting to note that most of the vorticity is in the wake region behind the particles. The downstream particles are thus subjected to vorticity generated by the upstream particles. The deformation of the advected vorticity around the downstream particle contributes to rotational forces on the particle [Eames & Hunt [36], Auton *et al.* [37]], whose magnitude can be estimated in terms of $\vec{u}\times\vec{\omega}$ where $\vec{u}$ and $\vec{\omega}$ are the undisturbed velocity and vorticity at the particular location.

Fig. 18 plots similar quantities but at a fixed time and for different volume fractions. Several points should be noted. First, the upstream propagation speed of the reflected shock is in general small, but appears to form quicker and travel upstream faster as the volume fraction increases. Comparing with the results of the Riemann problem shown in Fig. 6, it can be observed that the speed of the reflected shock is higher for the larger area reduction cases. The terminal Mach number of the reflected shock, is presented in Table VII, which can be compared with that shown in Table IV for the Riemann problem. It can be seen that the strength of the reflected shock, computed from numerical simulations is slightly higher than those predicted by the 1-D Riemann theory.

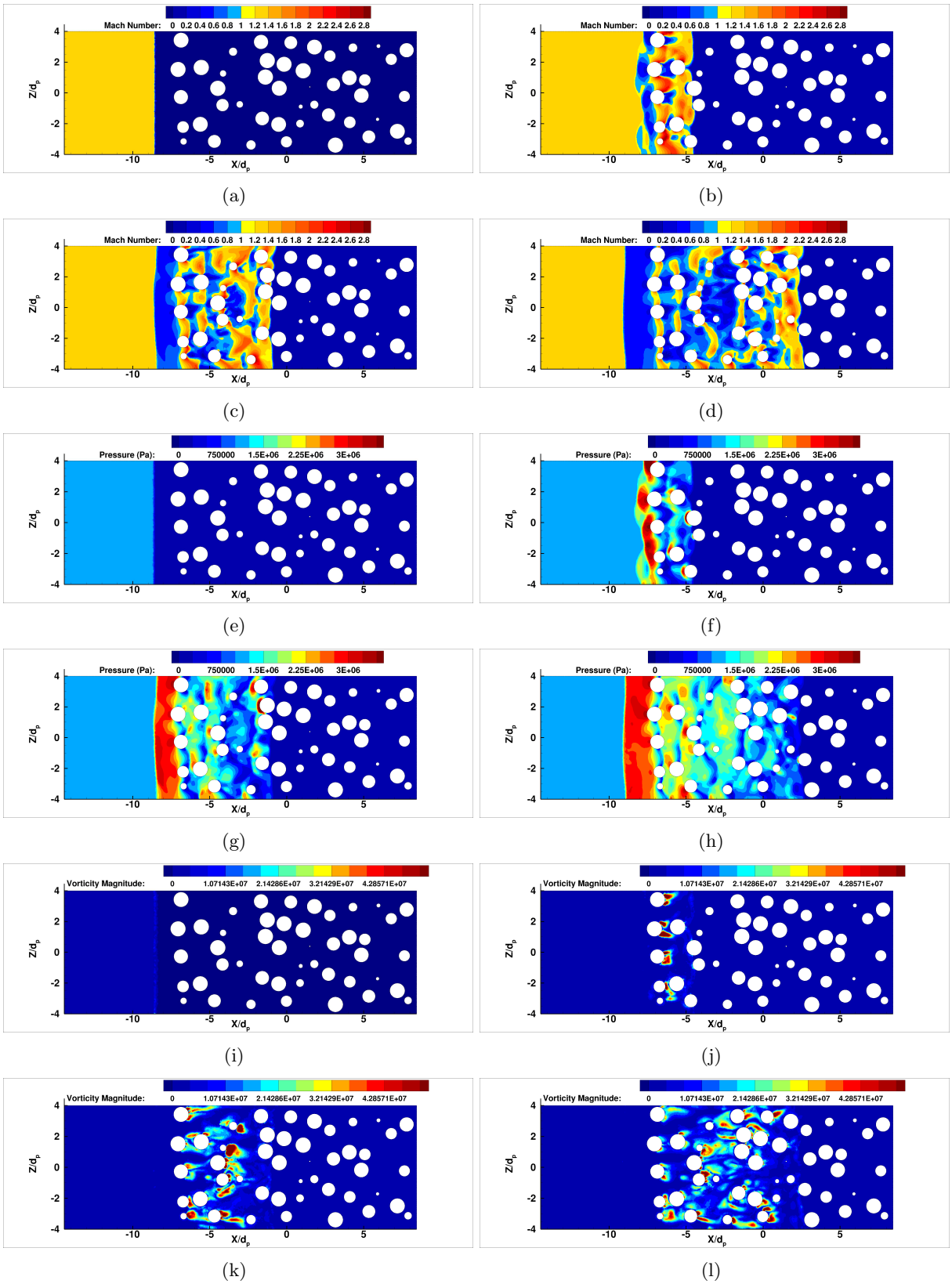

FIG. 17: Contour plot of Mach number (a-d); pressure (e-h); and vorticity (i-l) along the $x-z$ plane at $y=0$ for $M_s=3.0$ and $\phi_1=15\%$ at (a,e,i) $t/\tau=0$; (b,f,h) $t/\tau=4$; (c,g,k) $t/\tau=8$; (d,h,l) $t/\tau=12$.

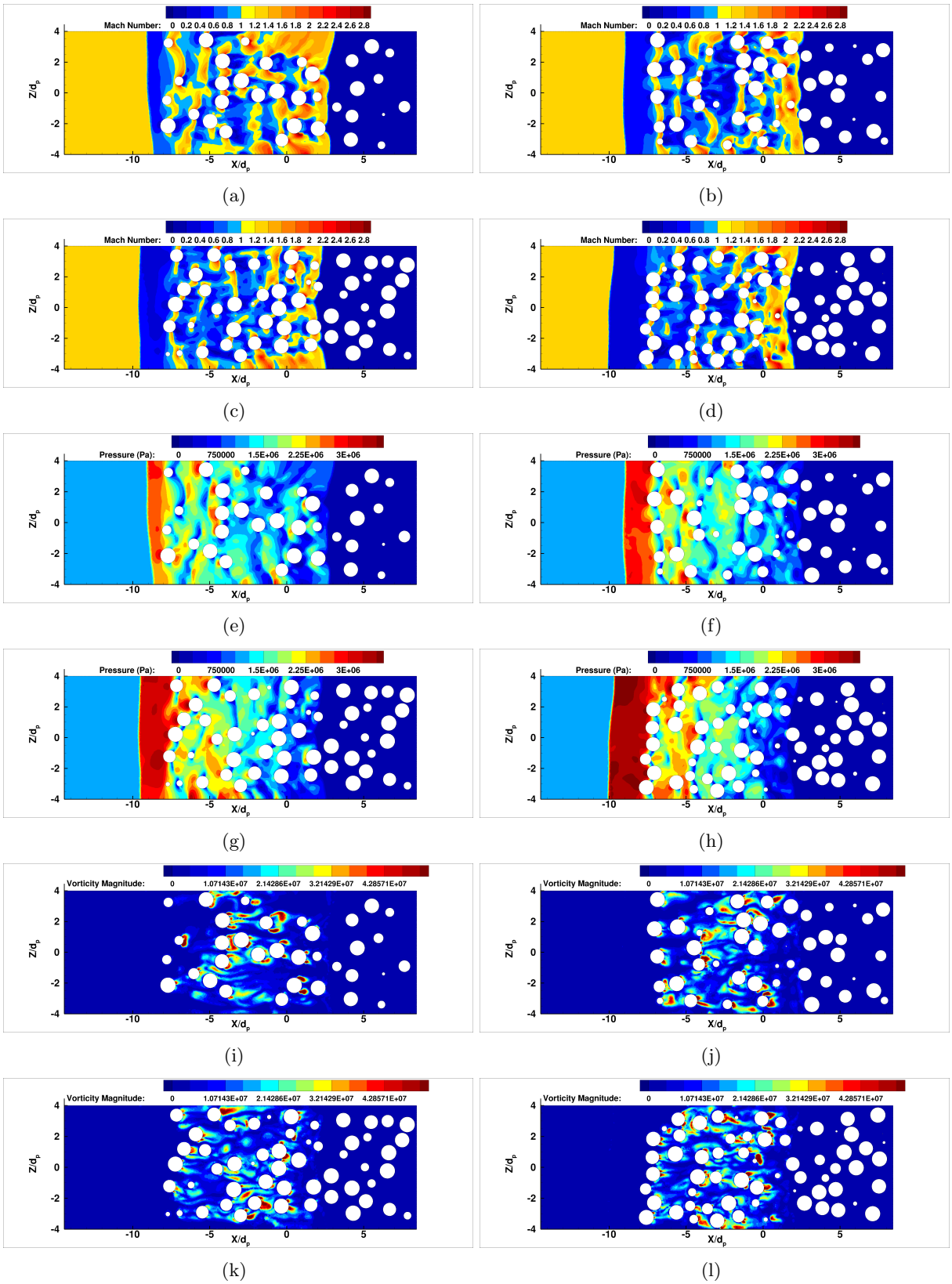

FIG. 18: Contour plot of Mach number (a-d); pressure (e-h); and vorticity (i-l) along the $x-z$ plane at $y=0$ for $M_s=3.0$ at $t/\tau=12$ for (a,e,i) $\phi_1=10\%$; (b,f,h) $\phi_1=15\%$; (c,g,k) $\phi_1=20\%$; (d,h,l) $\phi_1=25\%$.

4.4 Shock Attenuation through the Particle Bed

In this section we plot $y-z$-averaged flow quantities in the computational domain to determine, among other things, the strength of the transmitted shock. These cross-stream-averaged plots can be compared to those of the Riemann problem in order to better understand the impact of the particles on the flow, and to investigate the pressure attenuation or local amplification behind the particle (porous) barrier.

To compute averaged flow quantities, the computational domain is decomposed into 200 individual y-z slices. The flow field variables on the slices are then averaged to obtain a mean value of the quantities on the slice. This process yields a discrete set of averaged flow quantities that vary with time and the streamwise x-direction. If a flow variable is denoted as $F(x, y, z, t)$, then the process for determining the averaged value of the flow field variable on a slice is given by

$$\langle F \rangle(x,t) = \frac{1}{A_g} \int_{L_y} \int_{L_z} I_g(x,y,z) F(x,y,z,t)\, dydz. \tag{17}$$

where L_y and L_z are the size of the computational domain along the transverse directions. Here, $I_g(x, y, z)$ is the indicator function that identifies only the region occupied by the gas, outside the particle volume (i.e., $I_g = 1$ in the gas and $I_g = 0$ inside the particle). Thus, the integral is only over the cross-sectional area occupied by the gas and correspondingly $A_g = \int_{L_y} \int_{L_z} I_g(x, y, z)\, dydz$ is the cross-sectional area occupied by the gas.

The cross-stream-averaged pressure, density, and (u, v, w) velocity components normalized by post-shock values are shown in Figs. 19-21, respectively, and for the four volume fractions considered in this study. Here we consider the flow field results from the 200 2-D slices. Four representative times are used to show the evolution of the averaged flow field with time as the transmitted shock passes through the particle bed. Note that all four cases of volume fraction have the same post incident shock properties in the absence of a particle bed (i.e., same state ⑥), so the deviation from this state indicates how the flow in each particle bed differs.

The transmitted shock front can be seen in Fig. 19 as the location where the pressure rises rapidly from the ambient pressure state, which is the constant state on the right side of these figures. All quantities are scaled by their post incident shock value, and thus ahead of the reflected shock, all normalized quantities reach a constant value of 1.0 on the left. For 10% volume fraction, the pressure distribution shown in red of Fig. 19(a) is the initial condition with the shock discontinuity placed upstream of the particle bed. Hence the region between shocked and unshocked is clearly marked with a sharp pressure discontinuity. As the shock moves into the particle bed (green, blue, black) a coalesced bow shock begins to form upstream of the particle bed. The presence of this coherent bow shock can be seen as the steep pressure rise above the post shock pressure ahead of the particle bed. For the 15% volume fraction case, we can see in Fig. 19(b) that the pressure distributions are qualitatively similar to those in Fig. 19(a). The effect of the higher volume fraction in the bed can be seen in the peak upstream pressure increasing by about 20 percent compared to the peak in Fig. 19(a). In both these lower volume fraction cases, the pressure across the reflected shock continues to increase over the range of time considered. Thus, it can be concluded that the reflected shock is still developing towards a quasi-stationary state. For the 20% volume fraction case shown in Fig. 19(c), we can see that the pressure distributions are qualitatively similar to those of 10% and 15%. However, the pressure increase across the reflected shock upstream of the particle bed has reached a steady value, which is indicated by the near constant flat pressure distribution between the reflected shock and the front of the particle bed. This flattened peak is about 40% higher than the peak pressure of the 10% volume fraction case. This increase in pressure between

the reflected shock and the front of the particle bed with increasing particle volume fraction is in qualitative agreement with the corresponding behavior seen in the Riemann problem for sudden area reduction. The pressure ratios are given in Table VII for the four different volume fractions, which can be compared against the corresponding values presented in Table IV for the Riemann problem. From Fig 19, note that the growth of the coalesced bow shock is faster with increasing volume fraction. But this temporal development through coalescence of individual bow shocks is only a feature of the particle bed, as the reflected shock instantly forms in the case of the Riemann problem. Furthermore, the temporal development only pertains to the peak pressure, since in Fig. 19 the location of the reflected shock can be observed to steadily move upstream in all the cases considered. Similar to the previous pressure plot for 20% volume fraction, we see that the peak upstream pressure across the reflected shock increasing and plateauing in Fig. 19(d) for 25% volume fraction.

The pressure drops rapidly across the front face of the particle bed, which can be clearly observed in the higher volume fraction cases. The pressure continues to fall steadily across the bed and the pressure gradient increases with volume fraction. The pressure gradient within the bed appears to be nearly a constant in the high volume fraction cases, while in the low volume fraction cases the gradient seems to be slightly larger close to the front face of the particle bed.

The pressure jump on the right seen in all the plots is due to the transmitted shock. The pressure change across the shock front in all the cases experiences a decay with time as the transmitted shock front moves through the particle bed. Also, unlike the reflected shock, the pressure jump across the transmitted shock appears to occur over a region of finite thickness. From the Mach number contours shown in Figs. 17 and 18 it is clear that the transmitted shock is not planar. The undulations in the transmitted shock front as it diffracts around the bed of particles is responsible be the apparent finite thickness of the transmitted shock.

Fig. 20 shows the density variation with x/d_p at four different times for the four different particle bed volume fractions considered in this study. The density profiles are quite similar to those of pressure shown in Fig. 19. Again the signature of the reflected shock can be seen as the rapid increase in density upstream of the particle bed. The density of the gas rapidly decreases as it enters the particle bed, which is most evident at the higher volume fraction. Again the density linearly decreases within the upstream portion of the bed, and reaches a near constant value ahead of the transmitted shock. This behavior is entirely consistent with the density plot of the Riemann solution presented in Fig. 6. The region of linear density variation within the bed denotes the presence of a resonant expansion fan, whose thickness increases over time. However, such a constant state is not observed in the pressure distribution, since the decrease in pressure within the bed is due to both the resonant expansion fan and shocklet-induced energy dissipation. Nevertheless, the presence of a contact discontinuity cannot be discerned in the density plots, due to the very small value of the density jump that can be expected from the Riemann problem. The density jump seen in Fig. 20 across the reflected shock is consistent with the reflected shock Mach number presented in Table VII and similarly the density jump across the transmitted shock is consistent with the transmitted shock Mach number presented in Table VII.

The normalized streamwise velocity profiles are shown in Fig. 21. Here the velocity drops across the reflected and the transmitted shocks. As can be expected, the streamwise velocity increases sharply as the flow enters the bed of particles. Within the bed itself the velocity continues to increase. This increase is partially due to the resonant expansion fan and partially due to the dissipative decrease in pressure. We also calculated cross-stream averaged y and z components of velocities (but not shown here). They are typically limited to only 2% to 3% of the mean streamwise velocity. From statistical considerations we expect the ensemble-averaged transverse velocities to be zero and thus their small non-zero values are indicative of the effect of the finite

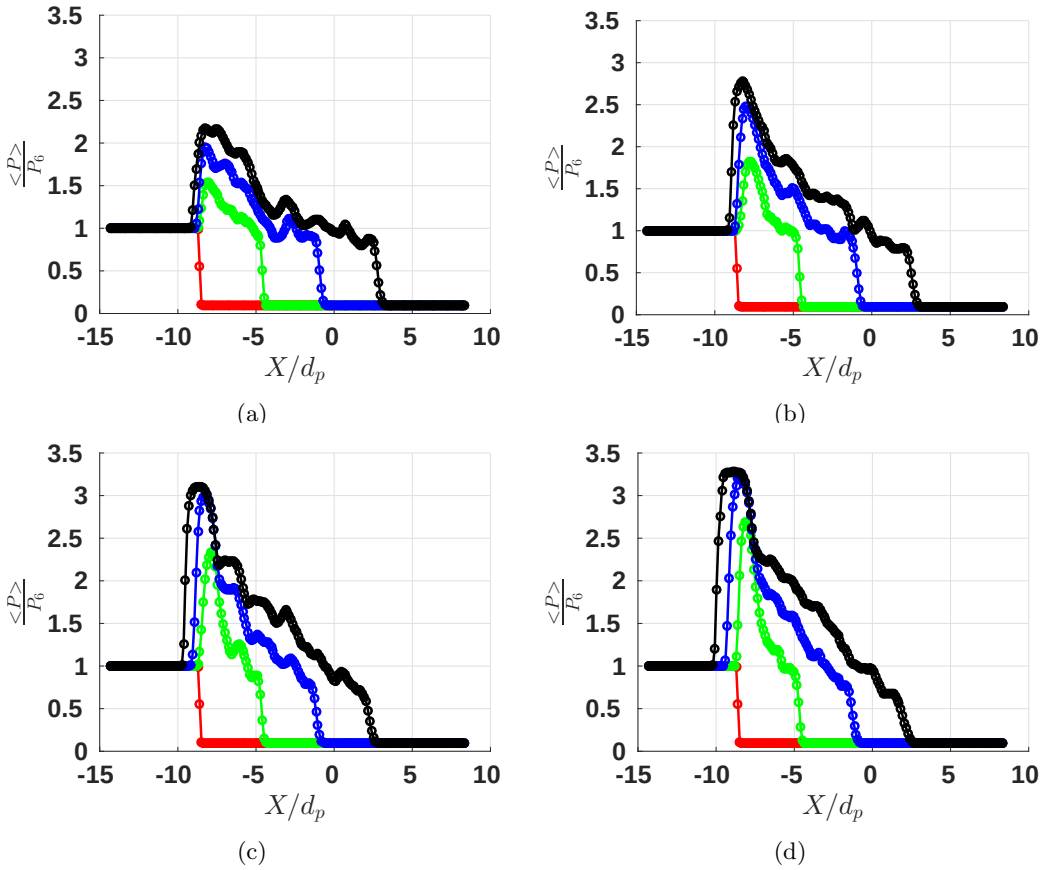

FIG. 19: Plot of normalized streamwise-averaged pressure, $\langle p \rangle / p_6$, in the random particle bed at four times and for (a) $\phi_1 = 10\%$, (b) $\phi_1 = 15\%$, (c) $\phi_1 = 20\%$, and (d) $\phi_1 = 25\%$. Times shown are $t/\tau = 0$ (red), $t/\tau = 4$ (green), $t/\tau = 8$ (blue), and $t/\tau = 12$ (black). The location of the imposed shock at $t/\tau = 0$ is approximately at $x/d_p = -9$. The particle bed begins at approximately $x/d_p = -8$.

dimension of the computational domain in the y and z directions. With a larger computational domain in the transverse directions the mean y and z velocities can be further decreased, however the computational cost will increase as well.

Ratios of pressure, density, and velocity behind the transmitted shock normalized by the post incident shock properties (P_2/P_6, ρ_2/ρ_6, and u_2/u_6) are presented in Table VII. These ratios help us quantify the dissipation inside the particle bed, since in the absence of particles the incident shock will be the transmitted shock. Note that the flow properties behind the transmitted shock in the case of the Riemann problem are nearly equal to the post incident shock properties. Also given in Table VII is the strength of the transmitted shock M_t, which can be compared with the Mach number of the transmitted shock for the Riemann problem given in Table IV. It is clear that the strength of the transmitted shock decreases as the volume fraction increases. We see from the table that the pressure drop across the particle bed varies between 13% for $\phi_1 = 10\%$ to 33% for $\phi_1 = 25\%$. Thus, there is a significant drop in the post-shock pressure of the transmitted shock front. This trend is consistent with the observed drop in the peak particle drag coefficients shown in Fig. 8. This decay of the transmitted shock is due to the added dissipation within the bulk of the particle bed, which will be further discussed in the following section.

TABLE VII: Flow properties across the domain from numerical simulations for different area reductions ; $M_s = 3$ and $t/\tau = 12$.

ϕ_1	M_r	M_t	P_5/P_6	ρ_5/ρ_6	u_5/u_6	P_4/P_6	ρ_4/ρ_6	u_4/u_6	P_2/P_6	ρ_2/ρ_6	u_2/u_6
10%	1.41	2.75	2.174	1.699	0.582	1.879	1.473	0.646	0.874	0.921	0.881
15%	1.59	2.64	2.778	2.016	0.412	1.811	1.379	0.659	0.799	0.880	0.822
20%	1.67	2.43	3.101	2.160	0.339	2.186	1.665	0.633	0.718	0.805	0.789
25%	1.72	2.34	3.277	2.229	0.304	2.216	1.606	0.562	0.678	0.761	0.751

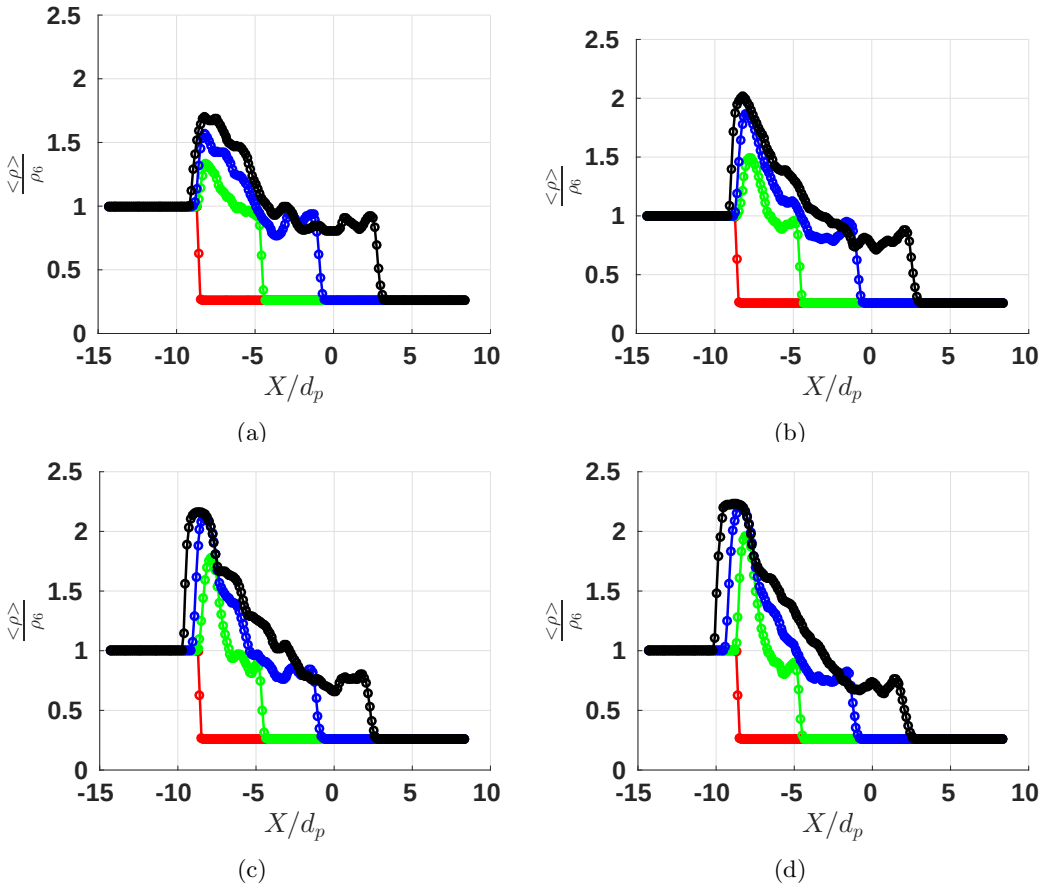

FIG. 20: Plot of normalized streamwise-averaged density, $\langle\rho\rangle/\rho_6$, in the random particle bed at four times and for (a) $\phi_1 = 10\%$, (b) $\phi_1 = 15\%$, (c) $\phi_1 = 20\%$, and (d) $\phi_1 = 25\%$. Times shown are $t/\tau = 0$ (red), $t/\tau = 4$ (green), $t/\tau = 8$ (blue), and $t/\tau = 12$ (black).

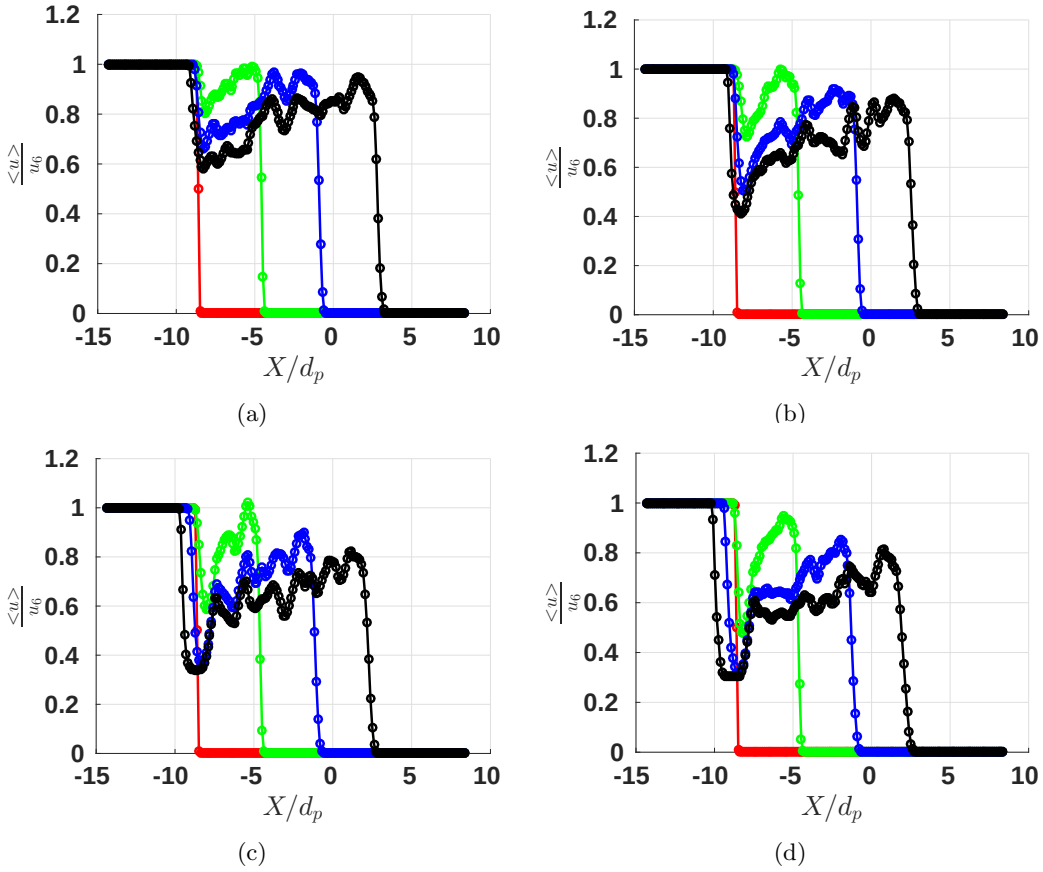

FIG. 21: Plot of normalized streamwise-averaged velocity, $\langle u \rangle / u_6$, in the random particle bed at four times and for (a) $\phi_1 = 10\%$, (b) $\phi_1 = 15\%$, (c) $\phi_1 = 20\%$, and (d) $\phi_1 = 25\%$. Times shown are $t/\tau = 0$ (red), $t/\tau = 4$ (green), $t/\tau = 8$ (blue), and $t/\tau = 12$ (black).

4.5 Approach to Equilibrium

The nozzle flow considered in Sec. 3 is similar to the problem of shock propagation through a bed of particles, except for the inviscid drag induced on the particles within the bed and the corresponding feedback effect on the flow. In the case of the 1-D nozzle flow shown in Fig. 4, the reflected and the transmitted shocks form very rapidly and propagate at constant velocity without any decay, and thus the 1-D nozzle flow can be considered to have reached its *equilibrium state*. A few additional points should be noted. In the inviscid nozzle limit there is dissipation of energy only at the reflected and the transmitted shocks, but the rate of energy dissipation remains a constant, since the reflected and the transmitted shock strengths remain the same over time; i.e., the reflected and the transmitted shocks are steady in respective frames attached to them. The equilibrium state of shock propagation in a 1-D nozzle flow is possible only when the dissipation rate is a constant. From Fig. 6 it is clear that the reflected shock will continue to move upstream at a constant speed, which is substantially lower than the speed of the transmitted shock.

The most significant difference between the 1-D nozzle solution and the results shown in Figs. 19 to 21 is the continued decay of the transmitted shock as it propagates deeper inside the particle bed. In contrast the transmitted shock in the 1-D nozzle is of constant strength. The difference between the two configurations is the presence of shocklets within the particle bed as the near uniform flow behind the transmitted shock negotiates around the random distribution of particles. These shocklets contribute to energy dissipation within the particle bed, which is in addition to dissipation that occurs at the reflected and transmitted shocks. As the transmitted shock propagates deeper into the particle bed, an increasing region of shocklets and energy dissipation forms within the bed swept by the transmitted shock. Thus, unlike in the 1-D nozzle flow where dissipation is limited to the reflected and the transmitted shocks and therefore remains a constant over time, in the case of a particle bed the rate of dissipation increases over time. This increasing total dissipation rate is related to (i) the steady reduction in the strength of the transmitted shock, (ii) the enhanced pressure gradient within the particle bed (in the 1-D nozzle flow the pressure gradient is only in the resonant expansion fan), and (iii) the next positive inviscid drag experienced by the particles over long time well after the passage of the transmitted shock.

We now can investigate conditions under which an *equilibrium state* will be approached in the case of shock propagation over a bed of particles. When the particle bed is of finite thickness (in other words in case of shock propagation past a frozen particle curtain), we can expect an equilibrium state to be approached over a very long time. As the transmitted shock moves past the finite-sized particle bed, subsequent evolution can be studied as a 1-D sudden expansion and the corresponding Riemann solution for the transmitted and reflected waves can be obtained. The reflected waves which propagate into the bed of particles will interact with the forward propagating contact discontinuity and the expansion fan, before reaching the front face of the particle bed. Similar reflections will occur for the contact as well as the expansion fan as they reach the back end of the particle bed. Over time there will be repeated reflections of waves inside the particle bed, with each reflections contributing to possible transmitted waves. The strength of these reflections decay over time and a final quasi-equilibrium state for the original reflected and the original transmitted shocks can be expected. This quasi-equilibrium state will depend on the net rate of dissipation that occurs within the bed of particle, which will approach a steady value as the internal reflections decay over time.

Two other factors that were not considered in the present simulations will affect the equilibrium state and its approach. It is appropriate to include viscous effects to represent the flow within the particle bed, even when the high-speed flow away from the particle bed can be satisfactorily represented by the Euler equations. The added viscous effect will enhance the aerodynamic force

on the particles, both during the transient state when the transmitted shock and the subsequent internally reflected waves propagate through the bed and during the long-term stationary state well after the passage of the transmitted shock. The enhanced dissipation within the bed of particles will decrease the equilibrium strengths of the reflected and transmitted shocks.

The relative importance of the viscous drag within the particle bed depends on the strength of the incident shock. In the present case of Mach 3 incident shock, the post-shock velocity is supercritical (i.e., greater than 0.6). As a result of the supercritical flow within the particle bed after the passage of the transmitted shock, shocklets are created within the bed, which result in dissipation and inviscid drag on the particles. Viscous effects will add to this dissipation and drag on the particles. With increasing incident shock Mach number the viscous contribution to dissipation and drag will become smaller. On the other hand, as the incident shock Mach number decreases below a certain critical value (which may depend on the particle volume fraction of the bed) the flow within the bed after the passage of the transmitted shock will remain entirely subsonic. In which case, the entire dissipation and drag on the particles is due to viscous effects. At such weak incident shock Mach numbers, an inviscid simulation result can be expected to be in closer agreement with the 1-D nozzle theory, as there is no added dissipation within the particle bed.

Substantial differences arise if the bed of particles is allowed to move downstream in response to the aerodynamic forces exerted on it (Wagner *et al.* [35], Ling *et al.* [25]). If the particle inertia is large, the particle acceleration will be slow and the velocity of the bed may not be significant until the transmitted shock is far downstream of the bed. Thus, as long as the transmitted shock is within the particle bed or only a short distance downstream, the results for a freely moving particle may still be close to those for a stationary bed. Over long time two effects contribute to a substantially different behavior. As the particles within the bed start to move downstream, the relative velocity between the particles and the surrounding gas decreases. As a result both the inviscid and viscous drag on the particles decrease over time, which will in turn modify the reflected and transmitted shocks. Also, experiments and simulations have shown that the thickness of the particle bed increases over time [25, 35, 38]), which will also influence the strength of the reflected and transmitted shocks.

Finally, let us consider the situation when the thickness of the particle bed is large. If we first restrict our attention to a strong incident shock in the inviscid limit, the following scenario can be envisioned. As the transmitted shock propagates through the bed its strength decreases due to shocklet-induced dissipation. As the transmitted shock strength decreases, there will be a location (L_{crit}) within the bed where the shock strength is sufficiently low that the flow after the shock passage is subcritical and does not support any internal shocklets within the bed. In this case, dissipation within the bed is limited to only upstream of L_{crit} and the extent of the bed beyond this point is unimportant. The transmitted shock strength at the very beginning will be as predicted by 1-D nozzle theory, but it will steadily decrease until the transmitted shock reaches L_{crit}. Beyond this point the transmitted shock strength will remain the same (as there is no additional dissipation), which is its inviscid equilibrium state. Correspondingly, the reflected shock will reach its equilibrium state as well. This equilibrium picture is pertinent only in an inviscid simulation. With viscous effects into account, dissipation rate will continue to increase within the bed and an equilibrium state cannot exist in the case of a very thick bed. The transmitted shock will be fully dissipated.

5 Conclusions

An investigation of a strong shock propagating through a random bed of spherical particles was presented. Three-dimensional numerical simulations were carried out and results for varying volume fraction at a fixed shock Mach number were given. We first computed the local volume fraction around each particle by means of Voronoi tessellation, and show significant variation in the local volume fraction. Knowledge of such information is useful when understanding the influence of nearest neighbors on global flow quantities such as drag. We next computed the unsteady inviscid streamwise and transverse drag coefficients for each particle in the random bed and found that the drag for each particle is strongly influenced by its nearest neighbors and the volume fraction. In particular, we show that the peak streamwise drag coefficient as a function of streamwise distance through the random bed decreases, and that the rate of decrease increases with volume fraction. We show that when properly scaled, the particle-particle variation of the peak streamwise drag coefficient can be well represented by a normal distribution. We also show that the peaks do not correlate with the local volume fraction or local Voronoi volume of a particle. Similar observations are made for the transverse particle forces. We also plotted the local Mach number and pressure contours for various volume fractions to explain the observed complex physical mechanisms occurring during the shock-particle interactions. Since the shock interaction with the random bed of particles lead to transmitted and reflected waves, we compute the average pressure to characterize the strength of the transmitted shock wave to study pressure attenuation through the particle bed. Finally, to better understand the complex wave dynamics in the particle bed, we compare solutions of the random bed to the Riemann problem of a shock propagating in a duct with a discontinuous cross-sectional area. Future work will include viscous effects as well as particle movement.

6 Acknowledgements

This work was supported in part by the U.S. Department of Energy, National Nuclear Security Administration, Advanced Simulation and Computing Program, as a Cooperative Agreement under the Predictive Science Academic Alliance Program, under Contract No. DE-NA0002378. TLJ was also supported in part by the Defense Threat Reduction Agency, Basic Research Award No. HDTRA1-14-1-0031 to University of Florida; SB was also supported in part by the Defense Threat Reduction Agency, Basic Research Award No. HDTRA1-14-1-0028 to University of Florida.

References

[1] Liu, Y., and Kendall, M. A. F., 2006. "Numerical analysis of gas and micro-particle interactions in a hand-held shock-tube device". *Biomedical Microdevices,* **8**(4), pp. 341–351.

[2] Igra, O., and Takayama, K., 1993. "Shock tube study of the drag coefficient of a sphere in a non-stationary flow". *Proceedings of the Royal Society of London A: Mathematical, Physical and Engineering Sciences,* **442**(1915), pp. 231–247.

[3] Britan, A., Elperin, T., Igra, O., and Jiang, J. P., 1995. "Acceleration of a sphere behind planar shock waves". *Experiments in Fluids,* **20**(2), pp. 84–90.

[4] Tanno, H., Itoh, K., Saito, T., Abe, A., and Takayama, K., 2003. "Interaction of a shock with a sphere suspended in a vertical shock tube". *Shock Waves,* **13**(3), pp. 191–200.

[5] Tanno, H., Komuro, T., Takahashi, M., Takayama, K., Ojima, H., and Onaya, S., 2004. "Unsteady force measurement technique in shock tubes". *Review of Scientific Instruments,* **75**(2), pp. 532–536.

[6] Sun, M., Saito, T., Takayama, K., and Tanno, H., 2005. "Unsteady drag on a sphere by shock wave loading". *Shock Waves,* **14**(1), pp. 3–9.

[7] Parmar, M., Haselbacher, A., and Balachandar, S., 2009. "Modeling of the unsteady force for shock–particle interaction". *Shock Waves,* **19**(4), pp. 317–329.

[8] Parmar, M., Haselbacher, A., and Balachandar, S., 2011. "Generalized basset-boussinesq-oseen equation for unsteady forces on a sphere in a compressible flow". *Phys. Rev. Lett.,* **106**, Feb, p. 084501.

[9] Parmar, M., Haselbacher, A., and Balachandar, S., 2012. "Equation of motion for a sphere in non-uniform compressible flows". *Journal of Fluid Mechanics,* **699**, 005, pp. 352–375.

[10] Lu, C., Sambasivan, S., Kapahi, A., and Udaykumar, H., 2012. "Multi-scale modeling of shock interaction with a cloud of particles using an artificial neural network for model representation". *Procedia IUTAM,* **3**, pp. 25 – 52. IUTAM Symposium on Linking Scales in Computations: From Microstructure to Macro-scale Properties.

[11] Regele, J., Rabinovitch, J., Colonius, T., and Blanquart, G., 2014. "Unsteady effects in dense, high speed, particle laden flows". *International Journal of Multiphase Flow,* **61**, pp. 1 – 13.

[12] Collins, T. J. B., Poludnenko, A., Cunningham, A., and Frank, A., 2005. "Shock propagation in deuterium-tritium-saturated foam". *Physics of Plasmas,* **12**(6), p. 062705.

[13] Sridharan, P., Jackson, T. L., Zhang, J., and Balachandar, S., 2015. "Shock interaction with one-dimensional array of particles in air". *Journal of Applied Physics,* **117**(7), p. 075902.

[14] Mehta, Y., Jackson, T. L., Zhang, J., and Balachandar, S., 2016. "Numerical investigation of shock interaction with one-dimensional transverse array of particles in air". *Journal of Applied Physics,* **119**(10), p. 104901.

[15] Mehta, Y., Neal, C., Jackson, T. L., Balachandar, S., and Thakur, S., 2016. "Shock interaction with three-dimensional face centered cubic array of particles". *Phys. Rev. Fluids,* **1**, Sep, p. 054202.

[16] Lefloch, P. G., and Thanh, M. D., 2003. "The riemann problem for fluid flows in a nozzle with discontinuous cross-section". *Commun. Math. Sci.,* **1**(4), 12, pp. 763–797.

[17] Krner, D., and Thanh, M. D., 2005. "Numerical solutions to compressible flows in a nozzle with variable cross-section". *SIAM Journal on Numerical Analysis,* **43**(2), pp. 796–824.

[18] Han, E., Hantke, M., and Warnecke, G., 2012. "Exact riemann solutions to compressible euler equations in ducts with discontinuous cross-section". *Journal of Hyperbolic Differential Equations,* **09**(03), pp. 403–449.

[19] Suzuki, K., Himeki, H., Watanuki, T., Abe, T., , , , and , 2000. "Experimental studies on characteristics of shock wave propagation through cylinder array". *title The Institute of Space and Astronautical Science report,* **676**, p. 1.

[20] Bulat, P., Ilyina, T., Volkov, K., Silnikov, M., and Chernyshov, M., 2016. "Interaction of a shock wave with an array of particles and effect of particles on the shock wave weakening". *Acta Astronautica*, pp. –.

[21] Naiman, H., and Knight, D. D., 2007. "The effect of porosity on shock interaction with a rigid, porous barrier". *Shock Waves,* **16**(4), pp. 321–337.

[22] Liou, M.-S., 1996. "A sequel to ausm: Ausm+". *Journal of Computational Physics,* **129**(2), pp. 364 – 382.

[23] Haselbacher, A., 2005. "A weno reconstruction algorithim for unstructured grids based on explicit stencil construction". *43rd AIAA Aerospace Sciences Meeting and Exhibit*.

[24] Ling, Y., Haselbacher, A., and Balachandar, S., 2009. "Transient phenomena in one-dimensional compressible gas–particle flows". *Shock Waves,* **19**(1), pp. 67–81.

[25] Ling, Y., Wagner, J. L., Beresh, S. J., Kearney, S. P., and Balachandar, S., 2012. "Interaction of a planar shock wave with a dense particle curtain: Modeling and experiments". *Physics of Fluids,* **24**(11), p. 113301.

[26] Ling, Y., Haselbacher, A., Balachandar, S., Najjar, F. M., and Stewart, D. S., 2013. "Shock interaction with a deformable particle: Direct numerical simulation and point-particle modeling". *Journal of Applied Physics,* **113**(1), p. 013504.

[27] Persson, P.-O., and Strang, G., 2004. "A simple mesh generator in matlab". *SIAM Review,* **46**, p. 2004.

[28] Si, H., 2015. "Tetgen, a delaunay-based quality tetrahedral mesh generator". *ACM Trans. Math. Softw.,* **41**(2), Feb., pp. 11:1–11:36.

[29] Akiki, G., Jackson, T. L., and Balachandar, S., 2016. "Force variation within arrays of monodisperse spherical particles". *Phys. Rev. Fluids,* **1**, Aug, p. 044202.

[30] Quintanilla, J., and Torquato, S., 1997. "Local volume fraction fluctuations in random media". *The Journal of Chemical Physics,* **106**(7), pp. 2741–2751.

[31] Yazdchi, K., Srivastava, S., and Luding, S., 2012. "Micromacro relations for flow through random arrays of cylinders". *Composites Part A: Applied Science and Manufacturing,* **43**(11), pp. 2007 – 2020.

[32] Matsumura, Y., and Jackson, T. L., 2014. "Numerical simulation of fluid flow through random packs of polydisperse cylinders". *Physics of Fluids,* **26**(12), p. 123302.

[33] Akiki, G., Jackson, T. L., and Balachandar, S., 2017. "Pairwise interaction extended point-particle model for a random array of monodispersespheres". *Journal of Fluid Mechanics,* **813**, 002, pp. 882–928.

[34] Boiko, V. M., Klinkov, K. V., and Poplavskii, S. V., 2004. "Collective bow shock ahead of a transverse system of spheres in a supersonic flow behind a moving shock wave". *Fluid Dynamics,* **39**(2), pp. 330–338.

[35] Wagner, J. L., Beresh, S. J., Kearney, S. P., Trott, W. M., Castaneda, J. N., Pruett, B. O., and Baer, M. R., 2012. "A multiphase shock tube for shock wave interactions with dense particle fields". *Experiments in Fluids,* **52**(6), pp. 1507–1517.

[36] EAMES, I., and HUNT, J. C. R., 1997. "Inviscid flow around bodies moving in weak density gradients without buoyancy effects". *Journal of Fluid Mechanics,* **353**, 12, pp. 331–355.

[37] Auton, T. R., Hunt, J. C. R., and Prud'Homme, M., 1988. "The force exerted on a body in inviscid unsteady non-uniform rotational flow". *Journal of Fluid Mechanics,* **197**, 12, pp. 241–257.

[38] Wagner, J. L., Beresh, S. J., Kearney, S. P., Pruett, B. O. M., and Wright, E. K., 2012. "Shock tube investigation of quasi-steady drag in shock-particle interactions". *Physics of Fluids,* **24**(12), p. 123301.